Effect of CeO_2 and MgO promoters on the performance of a Ni/Al_2O_3 catalyst in the steam reforming of biomass pyrolysis volatiles

Laura Santamaria, Maite Artetxe, Gartzen Lopez*, Maria Cortazar, Maider Amutio, Javier Bilbao and Martin Olazar

Department of Chemical Engineering University of the Basque Country UPV/EHU, P.O. Box 644 - E48080 Bilbao (Spain). gartzen.lopez@ehu.eus

Abstract

A Ni/Al_2O_3 catalyst has been modified incorporating CeO_2 and MgO promoters in order to improve its performance in the steam reforming of biomass pyrolysis volatiles. Ni/Al_2O_3, Ni/CeO_2-Al_2O_3 and Ni/MgO-Al_2O_3 catalysts have been prepared and fresh and deactivated catalysts have been characterized by N_2 adsorption/ desorption, X-ray Fluorescence (XRF), X-ray powder diffraction (XRD), Temperature Programmed Oxidation (TPO), Transmission Electron Microscopy (TEM) and a technique based on Fourier Transform Infrared Spectroscopy-Temperature Programmed Oxidation (FTIR-TPO). The results obtained revealed a similar initial activity for the three catalysts tested (conversion higher than 98 %), whereas stability has been greatly improved by incorporating CeO_2 as promoter, as it enhances the gasification of coke precursors. However, Ni/MgO-Al_2O_3 catalyst is slightly less stable than Ni/Al_2O_3, presumably as a result of its lower reducibility due to the formation of $MgAl_2O_4$ spinel phase. Catalysts deactivation has been associated with coke deposition, although sintering phenomenon became also evident when the Ni/CeO_2-Al_2O_3 catalyst was tested. The coke deposited on the catalysts does not present any specific morphology, which is evidence of its amorphous structure in the three catalysts studied.

Keywords

Hydrogen, steam reforming, biomass, nickel catalyst, promoters, ceria

1. Introduction

The depletion of fossil fuels and the environmental issues caused by their excessive use make necessary to explore alternative renewable and clean energy sources. In light of this situation, the thermochemical routes of biomass valorisation have attracted increasing attention [1-4]. Thus, pyrolysis [5-8] and gasification [9-11] of biomass have been extensively studied in literature in order to obtain high value added products, such as bio-oil, syngas and hydrogen.

Fossil fuel based processes are nowadays mostly used for producing hydrogen, whose demand is growing annually, with ammonia production and oil refining being the principal applications [12]. Besides, hydrogen is a clean fuel with greater energy density than other fuels [13] and surely will play an essential role as energy carrier in the future. The most studied routes for hydrogen production from biomass are steam gasification [9, 14-16] and steam reforming of the bio-oil obtained in biomass fast pyrolysis [17-20]. However, increasing attention has been recently paid to a strategy based on biomass pyrolysis and in-line steam reforming [21-23] due to several advantages compared to gasification and bio-oil steam reforming process. On the one hand, the use of two steps allows optimizing operating conditions in each step separately [24]. Besides, the temperature used in the reforming step is lower than that used in gasification, which attenuates catalyst deactivation by Ni sintering. Moreover, the main drawback of gasification lies in the formation of tar compounds together with the syngas [25, 26], which is avoided in the pyrolysis-reforming process, i.e., an almost tar free gas product is obtained [21]. On the other hand, the steam reforming of bio-oil requires the prior condensation of the volatile stream leaving the pyrolysis reactor, its storage and the subsequent volatilization steps, which involve operational problems and are energy demanding. Furthermore, the two-step process reforms all the oxygenate compounds

produced in the pyrolysis of biomass and avoids the re-polymerization of phenolic compounds occurring in the volatilization of the bio-oil.

Ni based commercial steam reforming catalysts have been widely used in the petrochemical industry for methane and naphtha reforming and they have also been proven to perform well as secondary catalysts in biomass gasification [27], bio-oil steam reforming [28], as well as in the in-line reforming of the volatiles formed in biomass pyrolysis [21]. Apart from Ni, other base metals (Co, Fe) and noble metals (Pt, Ir, Rh…) have been used as active phase in the reforming processes [29, 30]. The activity order of these metals is not clearly established in literature, with Ni being identified as the most appropriated one [13, 18, 28, 31] because of its activity for breaking C-C and O-H bonds and its moderate cost compare to noble metals. However, Ni is very active for the undesired methanation and coke formation reactions, and has low activity for the desired Water-Gas Shift reaction [18]. The most commonly used support for the Ni active phase has been Al_2O_3 [31] due to its high mechanical strength, tuneable textural properties and availability [18, 32]. However, the moderate acidity of Al_2O_3 support enhances the polymerization reactions leading to coke formation [33, 34]. Thus, the high coke formation rate on Ni/Al_2O_3 catalysts is the main challenge in bio-oil steam reforming process [18, 28, 35].

Modification of Ni/Al_2O_3 catalysts by incorporating metal oxide promoters (CeO_2, La_2O_3, MgO, CaO, ZrO_2…) has been widely studied in literature in order to increase their activity, reducibility, stability and regenerability in the reforming of oxygenate compounds [36-38]. Amongst the different metal oxides, CeO_2 has shown excellent properties to improve the thermal stability of the alumina by promoting the dispersion of Ni on the support, thereby favouring stronger metal-support interactions [39, 40]. Furthermore, CeO_2 enhances Water-Gas Shift reaction and favours coke gasification

because of its redox properties and high oxygen storage capacity [41, 42]. Furthermore, Chen et al. [43] studied methane dry reforming and observed that the formation of $CeAlO_3$ phase can inhibit the growth of graphitic carbon on the Ni surface. Alkali metals (MgO and CaO) have been incorporated into Ni/Al_2O_3 catalysts in order to reduce the acidity of Al_2O_3 support and decrease the coke formation rate. Besides, MgO favours H_2O adsorption and OH mobility on the surface, enhancing coke gasification [32, 44]. Sánchez-Sánchez et al. [45] reported that Mg addition leads to $MgAl_2O_4$ spinel phase formation, which modifies the interaction extent of Ni with Al_2O_3.

This study deals with hydrogen production from biomass based on a two-step in-line process. In the first step, biomass (pine sawdust) is pyrolyzed in a conical spouted bed reactor (CSBR) operating in continuous mode by feeding biomass and using steam as fluidizing agent. The volatile stream formed in the pyrolysis step is fed in-line into the second step, which is a catalytic fluidized bed reactor (CFBR). The good performance of the this CSBR-CFBR two-step process has already been proven when a commercial and synthesized Ni catalyst are used in the reforming step, as it allows attaining full conversion of the volatiles in the reforming step and high hydrogen yields at zero time on stream [21, 46]. However, catalyst deactivation is considerable, and therefore improvements in catalyst stability are required for increasing process viability. In order to improve Ni/Al_2O_3 catalyst stability, a study has been carried out on the effect CeO_2 and MgO promoters have on the evolution of conversion and product yields with time on stream, and they have been related to the catalyst deactivation by coke deposition and Ni sintering based on several catalyst characterization techniques.

2. Experimental

2.1. Materials

104 The biomass used is forest pine wood, whose main properties are summarized in
105 Table1. The biomass has been crushed, ground and sieved to a particle size in the 1-2
106 mm range in order to ease continuous feeding operation. The ultimate analysis has been
107 determined in LECO CHN-932 and VTF-900 elemental analyzers. The ultra-
108 microbalance SARTORIOUS M2P is on-line with a computer for the processing of the
109 data provided by the analyzer. The proximate analysis (volatile matter, fixed carbon and
110 ashes) has been determined in a thermogravimetric analyzer (TA Instrument TGA
111 Q5000IR). The higher heating value (HHV) has been measured in a Parr 1356
112 isoperibolic bomb calorimeter. As observed in Table 1, the empirical formula of the
113 biomass is $CH_{1.47}O_{0.67}$.

114 **Table 1**. Pine wood sawdust characterization.

Ultimate analysis (wt.%)	
Carbon	49.33
Hydrogen	6.06
Nitrogen	0.04
Oxygen	44.57
Proximate analysis (wt.%)	
Volatile matter	73.4
Fixed carbon	16.7
Ash	0.5
Moisture	9.4
HHV (MJ kg^{-1})	19.8

115

116 **2.2. Catalyst preparation and characterization**

117 Ni/Al_2O_3, Ni/CeO_2-Al_2O_3 and Ni/MgO-Al_2O_3 catalysts were prepared with 10 wt.%
118 nominal content of Ni. Prior to their synthesis, the γ-Al_2O_3 was pretreated by calcination
119 under air environment at 1000 ºC for 5 h to thermally stabilize the support thus avoiding

any possible phase change during the process, as well as improving the mechanical strength of the catalyst. The support was ground and sieved to a particle size in the 0.4-0.8 mm range. Ni/Al_2O_3 was prepared by wet impregnation of the support with an aqueous solution of $Ni(NO_3)_2.6H_2O$ (VWR Chemicals, 99 %). It was then dried at 120 ºC for 24 h, followed by calcination at 700 ºC for 3 h.

Modified supports were prepared by successive wet impregnation method. Prior to loading the Ni, calcined Al_2O_3 was modified with the promoter oxides (CeO_2, MgO) by impregnation in aqueous solutions of $Ce(NO_3)_3{\cdot}6H_2O$ and $Mg(NO_3)_2{\cdot}6H_2O$, respectively. The concentration of metal-promoter oxides onto the Al_2O_3 was fixed at 10 wt.%. The modified supports were dried overnight and calcined at 900 ºC for 3 h. Subsequently, Ni was impregnated with an aqueous solution of $Ni(NO_3)_2{\cdot}6H_2O$ (VWR Chemicals, 99 %) followed by drying at 120 ºC for 24 h and calcination at 700 ºC for 3 h.

The physical properties of the catalysts (BET surface area, pore volume and average pore diameter) were measured by N_2 adsorption-desorption (Micromeritics ASAP 2010). Prior to analysis, the samples were degassed under vacuum at 150 ºC for 8 h.

X-ray Fluorescence (XRF) spectrometry was used to measure the metal content of the catalysts. The chemical analysis of the samples was carried out under vacuum using a sequential wavelength dispersion X-ray fluorescence spectrometer (WDXRF), PANalytical AXIOS, equipped with Rh tube and three detectors. The samples were prepared mixing flux Spectromelt A12 from Merck (ref. No. 11802) with powder catalyst in a ratio of approximately 20:1. The samples were melted in an induction micro-furnace prior to chemical analysis.

143 Temperature Programmed Reduction (TPR) measurements were carried out in an
144 AutoChem II 2920 Micromeritics for determining the reduction temperature of the
145 different metal phases in the catalysts. In order to remove water or any other impurity,
146 the catalysts were thermally treated under helium stream at 200ºC. TPR analyses were
147 carried out from room temperature to 900ºC (heating rate of 5 ºC min^{-1}) in a H_2 stream
148 diluted in Ar (10 vol.%).

149 Crystalline structures of reduced and deactivated catalysts were analyzed by X-ray
150 powder diffraction (XRD) using Bruker D8 Advance diffractrometer with a $CuK_{\alpha 1}$
151 radiation. Scanning was conducted over 2θ = 10-80º range using 0.04º steps, with
152 measuring times being 12 s per step. Scherrer equation was used for calculating the
153 average Ni crystallite particle size, which allows determining metal dispersion
154 according to the method described by Miyazawa et al. [47].

155 Temperature Programmed Oxidation (TPO) was conducted for deactivated catalysts in
156 order to measure the amount of coke deposited and identify its possible nature and
157 location. A thermobalance (TGA Q5000TA Thermo Scientific) connected in-line to a
158 Blazer Instruments mass Spectrometer (Thermostar) was used, following a heating rate
159 of 5 ºC min^{-1} from 100 to 800 ºC in a stream of O_2 diluted in He. Prior to combustion,
160 the sample was stabilized with He stream at 100 ºC for 30 minutes and a final
161 temperature of 800 ºC was maintained for 30 minutes in order to ensure full coke
162 combustion.

163 TPO was also carried out following the coke combustion by FTIR spectrospopy in a
164 Nicolet 6700 spectrophotometer (Thermo) to determine the nature of the coke burned at
165 different temperatures. The deactivated catalysts were pelletized with KBr and
166 introduced into the catalytic chamber under vacuum at 100 ºC for 1 h in order to desorb

167 impurities. Combustion is carried out under air flow from 100 to 550 ºC at a rate of 5 ºC
168 $min^{-1,}$ and the final temperature was maintained for 1 h. Simultaneously, CO_2 signal was
169 recorded in a mass spectrometer (OmniStar ThermoStar).

170 Additionally, the nature of the coke deposited on the catalyst was studied by TEM
171 (transmission electron microscopy) images and SEM (scanning electron microscopy)
172 images, obtained by means of Phillips CM20 and JEOL JSM-6400, respectively.

173 **2.3. Experimental equipment, conditions and reaction indices**

174 A scheme of the bench scale reaction equipment used for the biomass pyrolysis-steam
175 reforming process is shown in Figure 1. The reaction system consists of two steps
176 connected in line: i) biomass pyrolysis in a conical spouted bed reactor; ii) in-line steam
177 reforming of the volatiles leaving the pyrolysis step in a fluidized bed reactor. The good
178 performance of the CSBR for biomass [48-51], tyre [52-54] and plastic [55-57]
179 pyrolysis has already been proven in previous studies.

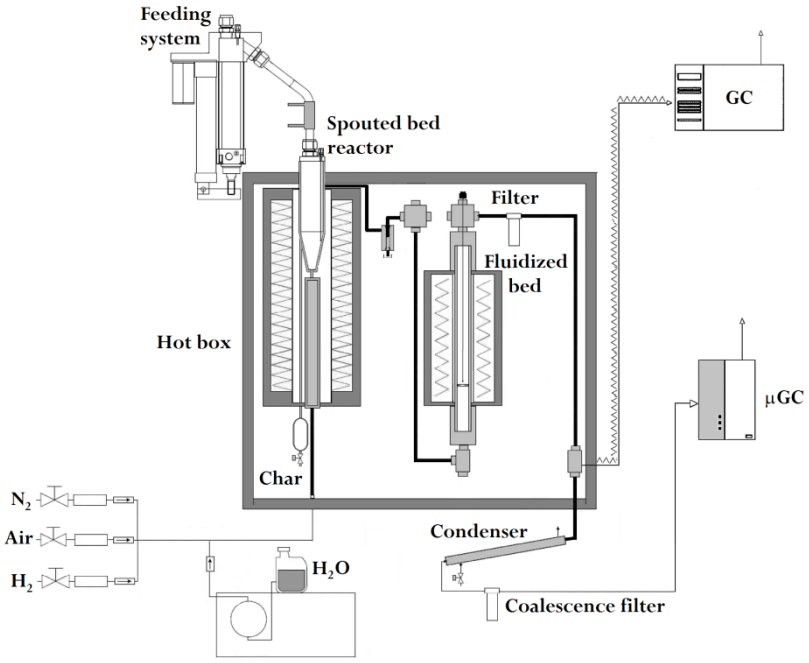

180

181 Figure 1. Scheme of the laboratory scale catalytic steam reforming plant.

182 Biomass was continuously fed (0.75 g min^{-1}) into the conical spouted bed reactor where
183 pyrolysis is carried out at 500 ºC for maximizing the volatile stream (gas and bio-oil)
184 yield [58].The bed was made up of 30 g of silica sand in the 0.3-0.35 mm range. Steam
185 has been used as fluidizing agent, with water flow rate being 3 mL min^{-1} to ensure
186 stable hydrodynamic performance. Thus, a steam/biomass ratio of 4 was used in all the
187 runs. A high precision Gilson 307 pump was used for measuring the water flow rate.
188 Prior to entering the reactor, it was vaporized and heated to the pyrolysis temperature by
189 means of a preheater. Both the preheater and the CSBR were placed inside a radiant
190 oven of 1250 W.

191 Biomass pyrolysis products were identified and quantified elsewhere [21, 58]. The inert
192 behaviour of steam in the biomass pyrolysis was previously verified, i.e., product
193 distribution is almost the same as when N_2 is used as fluidizing agent. Besides, the good
194 features of the conical spouted bed reactor, namely, short residence time, high heat and
195 mass transfer rates and rapid char removal, lead to high gas and bio-oil yields (overall
196 yield of 82 %). Thus, the main compounds in the volatile stream obtained in the first
197 step are CO (3.4 wt.%), CO_2 (3.3 wt.%), phenols (16.5 wt.%), ketones (6.4 wt.%),
198 saccharides (4.5 wt.%), furans (3.3 wt.%), acids (2.7 wt.%), alcohols (2.0 wt.%) and
199 aldehydes (1.9 wt.%). It should be noted that a water yield of 25 wt.% is obtained in
200 biomass pyrolysis, which also acts as reforming agent in the second step.

201 This volatile stream formed in the biomass pyrolysis reactor was fed into the fluidized
202 bed reactor placed in line, thus ensuring bed isothermicity and avoiding operational
203 problems encountered when operating in fixed bed reactors [59]. Before entering the
204 reactor, the volatile stream circulates throughout a filter and a cyclone in order to
205 eliminate possible char and sand particles entrained from the pyrolysis reactor. The total
206 mass in the fluidized bed reactor was 25 g, with catalyst particle size being 0.4-0.8 mm

and silica sand particle size 0.3-0.355 mm. The space-time used was 20 g_{cat} min $g_{volatiles}^{-1}$ for all the catalysts studied. The catalysts were reduced prior to the reforming process by an in situ reduction process at 710 ºC for 4 h under H_2 stream (10 vol.%) diluted with N_2. The reforming reaction was carried out at 600 ºC, as previous studies on this commercial catalyst showed no significant improvement when temperature was increased in the 600-700 ºC range [21]. The fluidized bed reactor was placed inside a radiant oven of 550 W.

Both reactors and its respective radiant ovens are located inside a convection oven kept at 270 ºC (Figure 1) in order to avoid the condensation of both the volatile stream formed in the pyrolysis reactor and the products formed in the fluidized bed reactor, as the latter should be avoided prior to analysis.

The product condensation system consists of a condenser cooled with tap water and a coalescence filter, which ensures non-condensable gases are clean for analysis. The product stream is analyzed in-line by: i) a Varian 3900 GC provided with HP-Pona column and flame ionization detector (FID); ii) a Varian 4900 microGC outfitted with four modules (Molecular sieve 5, Porapack, CPSil and Plot Alumina) and a thermal conductivity detector (TCD). The first sample of the product stream is taken at the fluidized bed reactor outlet, i.e., before condensing the products. The second one consisting of permanent gases is taken downstream the condensation system, which allows determining the compositions of the products not monitored by GC analysis. Thus, this system allows quantifying in line all the reforming products.

Reaction indices (conversion, carbon containing gaseous product yield and hydrogen yield) have been defined in order to quantify the performance of the different catalysts prepared. It should be noted that these indices are related to the reforming reactor, and

231 therefore the char formed in the pyrolysis reactor, which has been continuously
232 withdrawn, has not been considered.

233 Thus, conversion in the reforming reactor is defined as the ratio between the C moles in
234 the gaseous product (C_{gas}) stream and the C moles in the volatile stream at the fluidized
235 bed reactor inlet ($C_{volatiles}$):

236 $$X = \frac{C_{gas}}{C_{volatiles}} 100 \quad (1)$$

237 Likewise, the yield of any carbon containing gaseous product is defined as the ratio
238 between the molar flow rate of compound i (F_i) and the molar flow rate of the volatile
239 stream at the fluidized bed reactor inlet ($F_{volatiles}$):

240 $$Y_i = \frac{F_i}{F_{volatiles}} 100 \quad (2)$$

241 Regarding hydrogen yield, it is defined as follows:

242 $$Y_{H_2} = \frac{F_{H_2}}{F_{H_2}^0} 100 \quad (3)$$

243 where F_{H2} is the actual H_2 molar flow rate and F_{H2}^o is the maximum H_2 molar flow rate
244 allowable by stoichiometry. The following stoichiometry is considered for the steam
245 reforming of biomass pyrolysis volatiles:

246 $$C_n H_m O_k + (2n-k) H_2O \longrightarrow nCO_2 + (2n + m/2 - k) H_2 \quad (4)$$

247 **3. Results**

248 **3.1. Effect of CeO_2 and MgO promoters on Ni/Al_2O_3 catalyst**

The surface properties of the fresh catalysts (BET surface area (S_{BET}), pore volume (V_{pore}) and average pore diameter (d_{pore})) and their Ni content and metal dispersion (D_{XRD}) are set out in Table 2. As observed, the BET specific surface area decreases when CeO_2 or MgO is incorporated into Al_2O_3 support, from 76.2 to 65.7 and 63.9 m^2 g^{-1}, respectively. Likewise, pore volume also decreases, with this decrease being more significant for Ni/MgO-Al_2O_3 (from 0.39 to 0.27 cm^3 g^{-1}). It is well established that low metal oxide loadings in the support lead to atomic dispersion of Ce and Mg ions on the alumina, which does not have a significant effect on the textural properties [45]. However, an excess of Ce and Mg (up to 6 wt.% for CeO_2 [60] and 1 wt.% for MgO [61]) blocks the porous structure of the Al_2O_3 support, decreasing the surface area, as well as the pore volume of the catalysts. Furthermore, the formation of $MgAl_2O_4$ phase (detected by XRD analysis) enhances the decrease in pore volume observed for Ni/MgO-Al_2O_3 catalyst [62].

Table 2. Textural properties, nickel content and dispersion of the fresh catalysts.

Catalyst	Ni content wt.%	S_{BET} m^2 g^{-1}	V_{pore} cm^3 g^{-1}	d_{pore} Å	D_{XRD}[a] %
Ni/Al_2O_3	9.8	76.2	0.39	182.4	9.7
Ni/CeO_2-Al_2O_3	8.2	65.7	0.36	181.2	5.4
Ni/MgO-Al_2O_3	9.8	63.9	0.27	167.6	6.5

[a] Dispersion calculated by XRD based on Ni crystallite size [63].

The Ni content calculated by XRF analysis shows that the values obtained are close to nominal loading (10 wt.%), which is evident that the wet impregnation method used for catalyst preparation is adequate. Ni dispersion is calculated based on both the (97.1 nm)/(Ni particle size (nm) ratio [63] and Ni crystallite size by applying Scherrer equation to the diffraction peak at 2θ = 52º in the XRD analysis (associated with the Ni

phase). As observed, active phase dispersion values are quite low and they are even lower when CeO_2 and MgO are added as promoters. The low Ni dispersion obtained is presumably a consequence of the high Ni content and low surface area of the supports [64]. In fact, a lower metal dispersion is expected for Ni/CeO_2-Al_2O_3 and Ni/MgO-Al_2O_3 than for Ni/Al_2O_3 catalyst due to the lower BET surface area available for Ni deposition.

Figure 2 shows the XRD patterns of the three reduced catalysts. Diffraction lines at 2θ = 44º, 52º and 76º attributed to crystalline Ni phases are observed in all of them, which correspond to (1 1 1), (2 0 0) and (2 2 0) planes, respectively [65], whereas NiO is not detected, and therefore this specie is fully reduced. Regarding Ni/Al_2O_3 catalyst, typical diffraction peaks corresponding to Al_2O_3 support are detected, apart from those for Ni phase. However, $NiAl_2O_4$ spinel phase is not detected by this technique because its phase diffraction lines (2θ = 29º, 45º and 60º [66]) overlap those of Al_2O_3 phase [32, 67]. Likewise, $NiAl_2O_4$ spinel is not detected by XRD analysis to the reduced Ni/CeO_2-Al_2O_3 catalyst. However, $CeAlO_3$ spinel phase diffraction lines are identified at 2θ = 23º, 44º, 47º and 60º, as well as those of CeO_2 phase at 2θ = 28º, 33º, 47º and 56º. Osorio-Vargas et al. [60] related these CeO_2 peaks to fluorite structure, identified by planes (1 1 1), (2 0 0), (2 2 0) and (3 1 1), and they attributed the good segregation of CeO_2 on the Al_2O_3 support to this phase. Furthermore, the presence of $CeAlO_3$ is a consequence of solid-state reaction between Ce_2O_3 and Al_2O_3 above 600 ºC, with Ce_2O_3 being previously formed from CeO_2 in the presence of H_2 above 800 ºC [68]. Therefore, the presence of both phases is evidence that CeO_2 is partially reduced to Ce_2O_3 to form $CeAlO_3$ spinel phase when the catalyst has been reduced. Concerning Ni/MgO-Al_2O_3 catalyst, both $NiAl_2O_4$ spinel and $MgAl_2O_4$ spinel have been identified. However, both spinel phases have the same diffraction angles, and so their intensity cannot be

296 determined separately [69, 70]. Qiu et al. [71] also detected both spinel phases and they
297 concluded that $NiAl_2O_4$ spinel formation is inhibited and $MgAl_2O_4$ spinel formation
298 enhanced when the MgO content is below 7 wt.%.

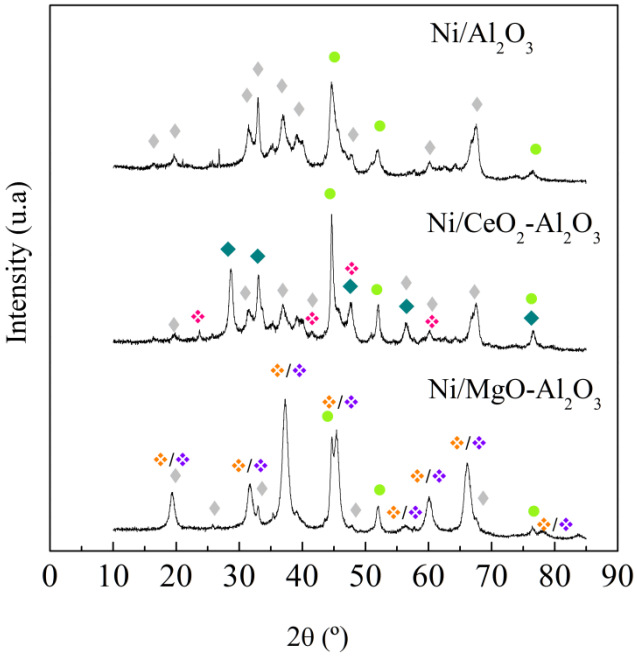

299

300 Figure 2. XRD patterns of the reduced catalysts. Crystalline phases: (●) Ni (♦) Al_2O_3
301 (❖) $CeAlO_3$ (◆) CeO_2 (❖) $MgAl_2O_4$ (❖) $NiAl_2O_4$.

302

303 Figure 3 shows the TPR profiles of Ni/Al_2O_3, Ni/CeO_2-Al_2O_3 and Ni/MgO-Al_2O_3
304 catalysts. Regarding Ni/Al_2O_3 catalyst, two main reduction peaks are observed at 620 ºC
305 and 780 ºC. Besides, a small peak is observed at lower temperatures, which presumably
306 corresponds to the reduction of NiO with little or no interaction with Al_2O_3 [32].
307 Moreover, the peak at 620 ºC can be associated with NiO strongly interacting with
308 Al_2O_3 support, which at higher temperature corresponds to Ni integrated in the $NiAl_2O_4$
309 spinel phase [72]. Concerning Ni/CeO_2-Al_2O_3 catalyst, it can be seen that these
310 reduction peaks shift to lower temperatures (550 ºC and 710 ºC) when CeO_2 is used as
311 promoter, indicating that the presence of CeO_2 weakens the interation of NiO with

312 Al_2O_3 [60]. It is to note that another small reduction peak is observed at higher
313 temperature (> 800 ºC) associated with the reduction of bulk ceria crystallites related to
314 $CeAlO_3$ formation [73]. Concerning Ni/MgO-Al_2O_3 catalyst, the low capacity for
315 reduction of the catalyst prepared is noteworthy, as evidenced by a small peak at 550 ºC
316 related to NiO interacting with Al_2O_3 support. Besides, another peak at high
317 temperature (> 800 ºC) is observed related to the Ni incorporated into $MgAl_2O_4$ spinel,
318 which is difficult to reduce [32, 62].

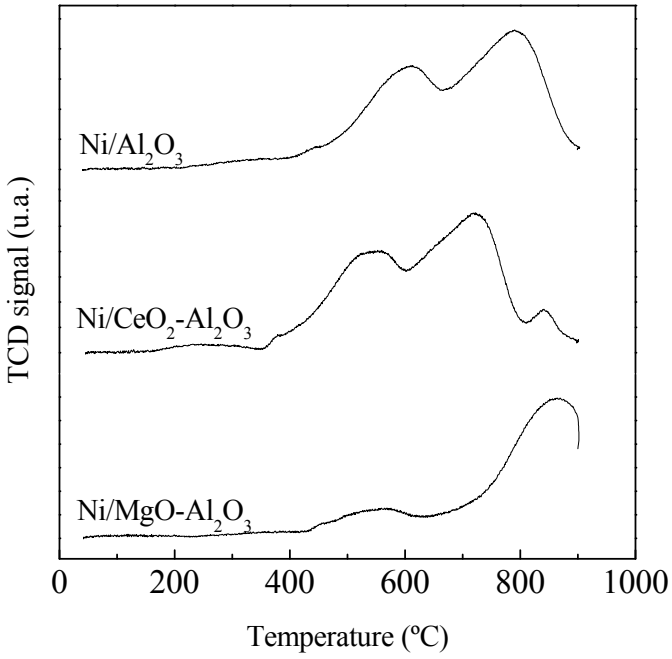

319

320 Figure 3. TPR profiles of Ni/Al_2O_3, Ni/CeO_2-Al_2O_3 and Ni/MgO-Al_2O_3 catalysts.

321 **3.2. Comparison of the catalysts performance**

322 Figure 4 displays the evolution of conversion (Eq. (1)) with time on stream for the three
323 catalysts tested. It is to note that the times on stream for a conversion to be lowered to
324 80 % depend on the catalyst used (98, 155 and 91 min for Ni/Al_2O_3, Ni/CeO_2-Al_2O_3 and
325 Ni/MgO-Al_2O_3, respectively), i.e., the Ni/CeO_2-Al_2O_3 catalyst allows operating for

longer periods with high conversion values. Furthermore, almost full conversion is obtained at zero time on stream, with reforming conversion of biomass pyrolysis volatiles being above 98 % for the three catalysts prepared. As observed, Ni/MgO-Al_2O_3 is the less stable one, with conversion decreasing from 99.1 % at zero time on stream to 56.6 % for 106 min on stream. This low stability of the Ni/MgO-Al_2O_3 catalyst is related to the low catalyst reducibility observed by TPR analysis, since less Ni active phase on the catalyst leads to faster catalyst deactivation. Likewise, Garcia et al. [69] tested different Ni/Al_2O_3 catalysts promoted with MgO and observed lower stability for the catalyst in which the spinel phase was formed and reducibility was limited. Furthermore, although Ni/Al_2O_3 catalyst shows an initial stable period (40 min), its deactivation rate is similar to that observed for Ni/MgO-Al_2O_3, with conversion decreasing from 97.8 % at 40 min on stream to 73.9 % at 103 min. However, it is clearly observed that incorporating CeO_2 as promoter the catalyst deactivation rate is attenuated considerably, with conversion decreasing from 99.5 % at zero time on stream to 94 % for 104 min, and conversion being still 60 % at 200 min. The good stability of Ni/CeO_2-Al_2O_3 catalyst for oxygenate compound reforming has been reported in the literature, and is related to CeO_2 redox properties and its high oxygen storage capacity, as well as to the enhancement of water adsorption by inhibiting coke formation and evolution on the catalyst surface [42, 45].

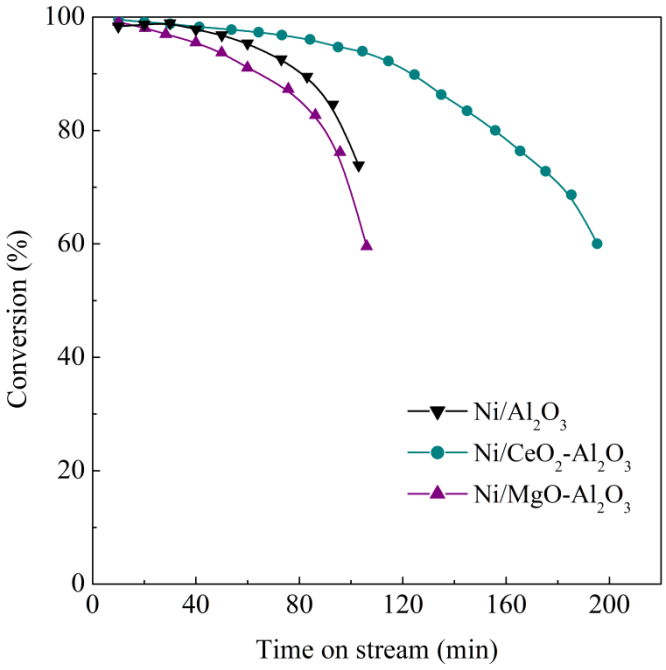

345

346 Figure 4. Evolution of conversion with time on stream for the different catalysts.

347 Figure 5 shows the evolution of H_2 yield (calculated based on the maximum allowable
348 by stoichiometry, Eq. (3)) and other gaseous compound yields (Eq. (2)) with time on
349 stream for Ni/Al_2O_3 (Figure 5a), Ni/CeO_2-Al_2O_3 (Figure 5b) and Ni/MgO-Al_2O_3 (Figure
350 5c) catalysts. As observed, as time on stream is increased H_2 and CO_2 yields decrease
351 for the three catalysts, which is evidence of a lower extension of reforming and water-
352 gas shift reactions when the catalyst is deactivated. Besides, this decrease is more
353 pronounced for Ni/MgO-Al_2O_3 catalyst (Figure 5c). Thus, H_2 yield decreases from 93.7
354 to 44.3 % and the one of CO_2 from 91.2 to 48.4% for 106 min. It is to note that an initial
355 period has been observed for Ni/Al_2O_3 catalyst (Figure 5a), with H_2 yield (93.8 %) and
356 CO_2 yield (91.6 %) being almost constant for 40 min. However, after this period the
357 decrease in H_2 and CO_2 yields is more pronounced than for Ni/CeO_2-Al_2O_3 catalyst
358 (Figure 5b). Catalyst deactivation rate increases with time on stream for the three
359 catalysts studied; that is, there is an autocatalytic effect suggesting that non-converted

oxygenates are the main coke precursor because the deactivation is faster as their concentration in the reaction medium is higher.

Regarding CO yield, it is almost constant for Ni/Al_2O_3 catalyst, but increases slightly with time on stream for $Ni/MgO-Al_2O_3$ and in a more pronounced way for $Ni/CeO_2-Al_2O_3$, which is due to a balance between the lower extension of reforming and water-gas shift reactions and its formation by cracking (especially decarbonylation) reactions. Comparing the CO yields obtained with the three catalysts, on one hand, the lower value of CO yield obtained when Ni/Al_2O_3 catalyst is used is evidence of the lower extension of the water-gas shift reaction when the support is modified. On the other hand, the higher value of CO yield obtained when $Ni/CeO_2-Al_2O_3$ is used is related to the redox capacity of this catalyst, i.e., its reduction to CeO_{2-x} by unreacted hydrocarbons (C_xH_{1-x}) and reoxidation back to CeO_2 by CO_2 leads to the formation of CO in both steps [73].

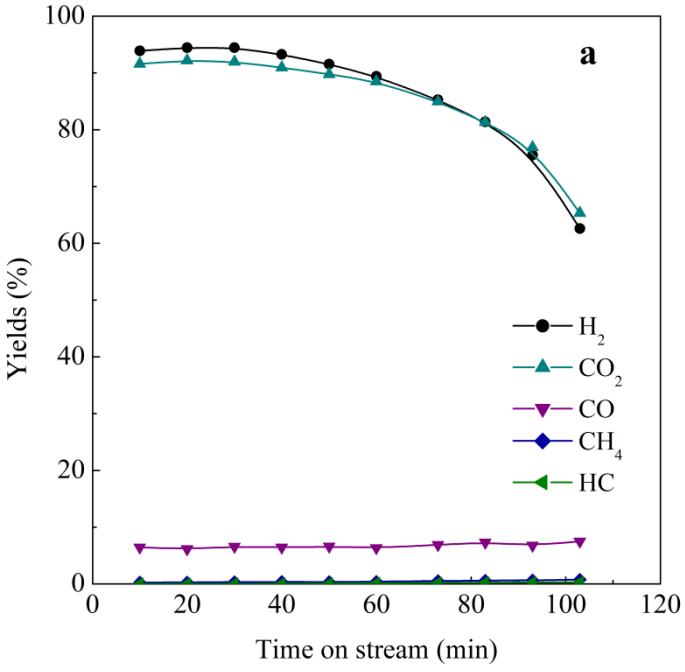

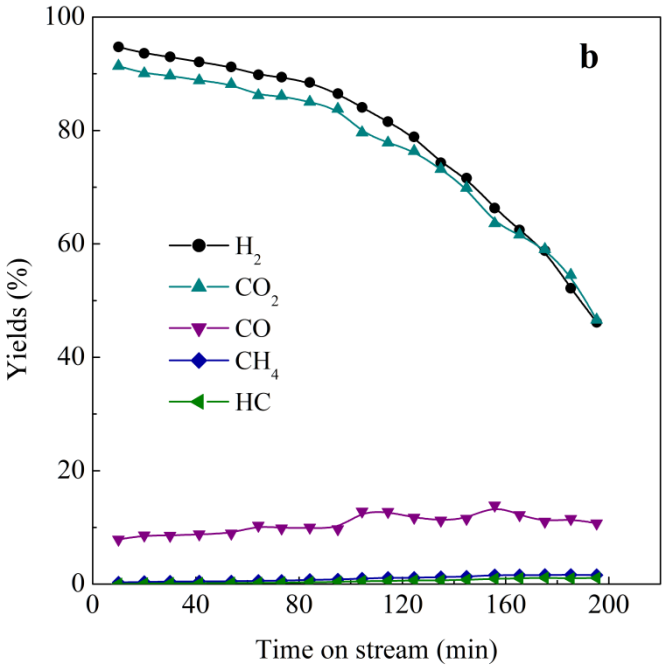

374

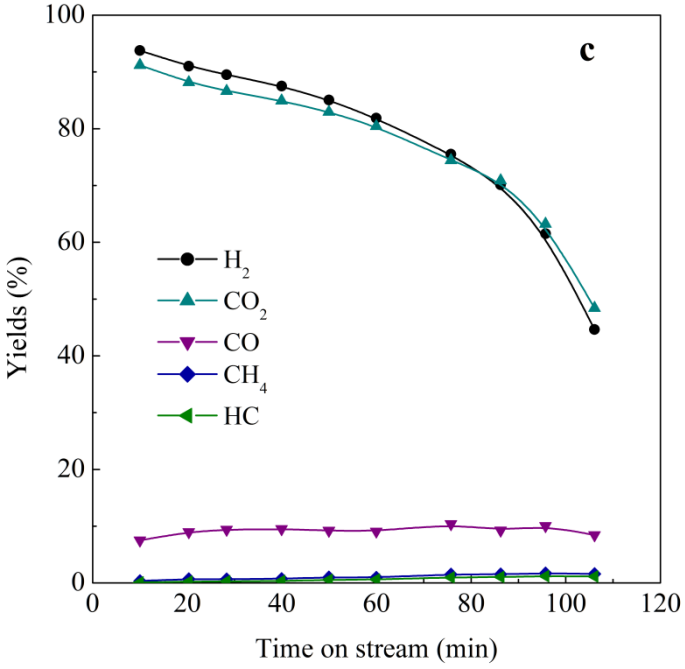

375

376 Figure 5. Evolution of H_2 and other gaseous compound yields with time on stream for

377 Ni/Al_2O_3 (a), Ni/CeO_2-Al_2O_3 (b) and Ni/MgO-Al_2O_3 (c) catalysts.

Concerning CH_4 and light hydrocarbons yields, they increase slightly as deactivation proceeds, but their yields are below 2 % for the three catalysts. Therefore, oxygenate cracking reactions hardly occur under reaction conditions, even when the catalysts are deactivated and reforming reactions are attenuated.

Several studies dealing with the dry reforming of hydrocarbons relate the good stability of Ni/CeO_2-Al_2O_3 catalysts to the formation of $CeAlO_3$ spinel, which plays a key role in the removal of coke precursors by the following reaction mechanisms [43, 73]: i) $CeAlO_3$ spinel may react with CO_2 to form CO and CeO_2; and ii) CeO_2 oxidizes the coke precursors located at the Ni-support boundary and restores $CeAlO_3$ sites. Besides, this mechanism for the removal of coke precursors may also explain the higher CO yields obtained using Ni/CeO_2-Al_2O_3 catalyst.

3.3. Catalyst deactivation

One of the main concerns of bio-oil steam reforming process is the fast catalyst deactivation, generally caused by coke deposition or Ni sintering [18, 74]. In order to overcome or minimize this deactivation, it is of uttermost importance to understand the mechanism leading to catalyst deactivation. Accordingly, this section deals with the decline in the catalyst textural properties, modifications on different crystal phases and the nature and location of the coke deposited.

Table 3 shows the textural properties of deactivated Ni/Al_2O_3, Ni/CeO_2-Al_2O_3 and Ni/MgO-Al_2O_3 catalysts. A comparison of these properties with those shown in Table 2 for the fresh catalysts reveals that the BET surface area is almost the same for the Ni/Al_2O_3 catalyst (76.2 and 74.7 m^2 g^{-1} for the fresh and deactivated catalysts, respectively), whereas it decreases slightly for Ni/CeO_2-Al_2O_3 (from 65.7 to 58.6 m^2 g^{-1}) and Ni/MgO-Al_2O_3 (from 63.9 to 57.5 m^2 g^{-1}). Furthermore, pore volume and pore

diameter decrease for the three catalysts due to the coke deposited, which is evidence that the coke may block the biggest pores either fully or partially, with the latter causing a decrease in the diameter to access the pore.

Table 3. Textural properties of the deactivated catalysts and Ni crystallite size (d_{Ni}).

Catalyst	S_{BET} $m^2\ g^{-1}$	V_{pore} $cm^3\ g^{-1}$	d_{pore} Å	d_{Ni} (fresh) nm	d_{Ni} (deact.) nm
Ni/Al_2O_3	74.7	0.29	153.3	10	13
Ni/CeO_2-Al_2O_3	58.6	0.23	165.2	18	31
Ni/MgO-Al_2O_3	57.5	0.20	140.0	15	19

Figure 6 shows XRD patterns of the three deactivated catalysts. It is to note that no significant differences are observed when they are compared with the XRD profiles of the fresh catalysts (Figure 2). Besides, diffraction lines attributed to Ni crystalline phases are observed for the three catalysts studied, but those of NiO are not identified, which reveals that catalyst deactivation is not caused by the active phase oxidation. The deactivated Ni/CeO_2-Al_2O_3 catalyst records another diffraction line representative of $CeAlO_3$ spinel phase at $2\theta = 34º$, which does not appear in fresh catalyst, indicating the formation of this spinel phase under reaction conditions. In order to determine catalyst irreversible deactivation by Ni sintering, Ni crystallite size has been calculated for fresh and deactivated catalysts (Table 3), applying the Scherrer equation for the diffraction peak at $2\theta = 52º$. As observed in Table 3, the Ni crystallite size for Ni/Al_2O_3 and Ni/MgO-Al_2O_3 catalysts does not increase considerably, and therefore the fast deactivation observed for these catalysts is not due to Ni sintering. In the case of Ni/CeO_2-Al_2O_3 catalyst, the Ni crystallite size increases from 18 to 31 nm, which suggests that certain sintering occurs under the reaction conditions. Navarro et al. [62] showed also a higher Ni particle size under reaction conditions when they used CeO_2 as

promoter for Ni/Al_2O_3, and they relate it to the poor Ce particle dispersion in the catalyst, which cannot avoid Ni sintering and stabilize the catalyst.

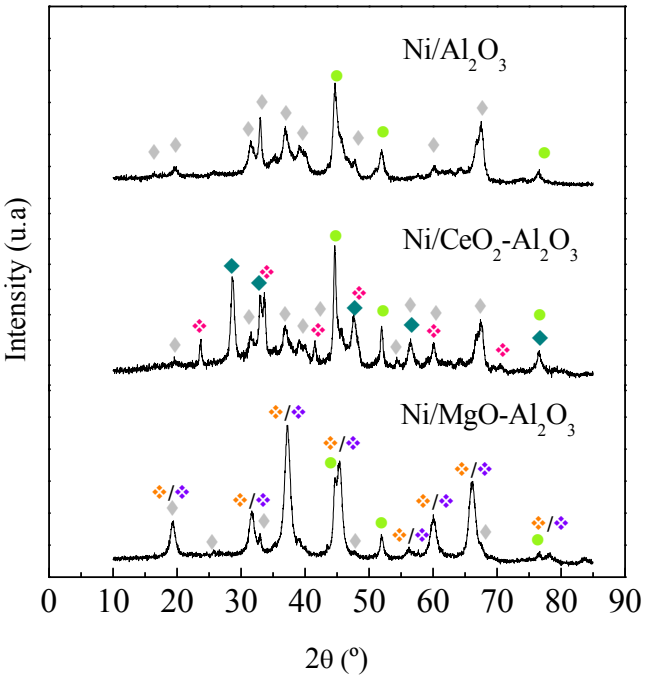

Figure 6. XRD patterns of the deactivated catalysts. Crystalline phases: (●) Ni (◆) Al_2O_3 (❖) $CeAlO_3$ (◆) CeO_2 (❖) $MgAl_2O_4$ (❖) $NiAl_2O_4$.

Therefore, as Ni particle sintering is not significant for Ni/Al_2O_3 and $Ni/MgO\text{-}Al_2O_3$ catalysts, the main cause of catalyst deactivation with time on stream is the coke deposited on these catalysts. In the case of $Ni/CeO_2\text{-}Al_2O_3$, although sintering may affect catalyst stability, the influence of the coke deposited on this catalyst will be also analysed. Thus, temperature programmed oxidation (TPO) of the coke deposited has been carried out in order to analyze the amount and the nature and location of the coke deposited. The amount of the coke deposited on the three catalysts has been summarized in Table 4 and their TPO profiles have been plotted in Figure 7. As aforementioned, the time on stream of each catalyst was not the same (103, 200 and 106 min for Ni/Al_2O_3, $Ni/CeO_2\text{-}Al_2O_3$ and $Ni/MgO\text{-}Al_2O_3$, respectively). Therefore, in order to compare the

amount of coke deposited on the different catalysts, the average coke deposition rate has been defined as follows:

$$\overline{r}_{coke} = \frac{W_{coke}/t}{W_{catalyst}\, m_{biomass}} \quad (5)$$

with $W_{catalyst}$ and W_{coke} being the catalyst and coke masses, respectively, $m_{biomass}$ the biomass mass flow rate in the feed and t the reaction time in each run.

Table 4 shows a lower average coke deposition rate for Ni/CeO_2-Al_2O_3 catalyst (0.31 $mg_{coke}\, g_{cat}^{-1}\, g_{biomass}^{-1}$), which is consistent with the lower deactivation observed when the evolution of conversion and product yields with time on stream has been monitored (Figures 4 and 5, respectively). This is an especially relevant result, since the Ni/CeO_2-Al_2O_3 catalyst has been exposed to higher partial pressures of non-converted oxygenate compounds for longer reaction times, and the extension of coke formation is therefore higher. Similarly, the fast decrease in conversion and H_2 and CO_2 yields with time on stream observed for Ni/MgO-Al_2O_3 is related to the higher average coke deposition rate (0.77 $mg_{coke}\, g_{cat}^{-1}\, g_{biomass}^{-1}$) when this catalyst is used. Furthermore, significant differences on the coke nature and location are observed depending on the promoter used (Figure 7). The nature and location of the coke deposited is ascertained in the literature based on the combustion temperature of the different coke fractions observed in the TPO profiles [32, 75, 76], as follows: i) the coke that burns below 500 ºC is related to the amorphous coke or the one deposited on Ni particles catalyzing its oxidation. This coke fraction encapsulates Ni particles, hindering the access of reactants to the active sites, and is therefore the main responsible for catalyst deactivation; ii) higher combustion temperatures are associated with the combustion of structured or filamentous coke, with less influence on catalyst deactivation. Regarding the Ni/Al_2O_3 catalyst (Figure 7), two clearly defined peaks are observed, the first one at 480 ºC

associated with amorphous coke and the second one at 600 ºC related to a more structured coke. Similarly, both peaks are observed in the case of Ni/MgO-Al_2O_3, with the one at low temperature being more pronounced. Therefore, it seems that the incorporation of MgO as promoter inhibits the evolution of the coke towards a more structured material, as has also been observed by other authors [62]. As concerns the Ni/CeO_2-Al_2O_3 catalyst, the coke deposited on this catalyst burns at a lower temperature (the main peak below 400 ºC), which is related to CeO_2 enhancing coke gasification during the steam reforming of biomass pyrolysis volatiles and coke oxidation during its combustion. It is widely reported in the literature [18, 43, 45] that CeO_2 incorporation as promoter enhances water adsorption and provides redox properties to the support, which increase the oxygen available on the surface, thus favouring coke gasification and inhibiting its growth and evolution towards a more structured coke.

Table 4. Coke content and average coke deposition rate for the three catalysts.

Catalyst	C_c wt.%	r_{coke} $mg_{coke}\, g_{cat}^{-1}\, g_{biomass}^{-1}$
Ni/Al_2O_3	2.84	0.37
Ni/CeO_2-Al_2O_3	4.52	0.31
Ni/MgO-Al_2O_3	6.15	0.77

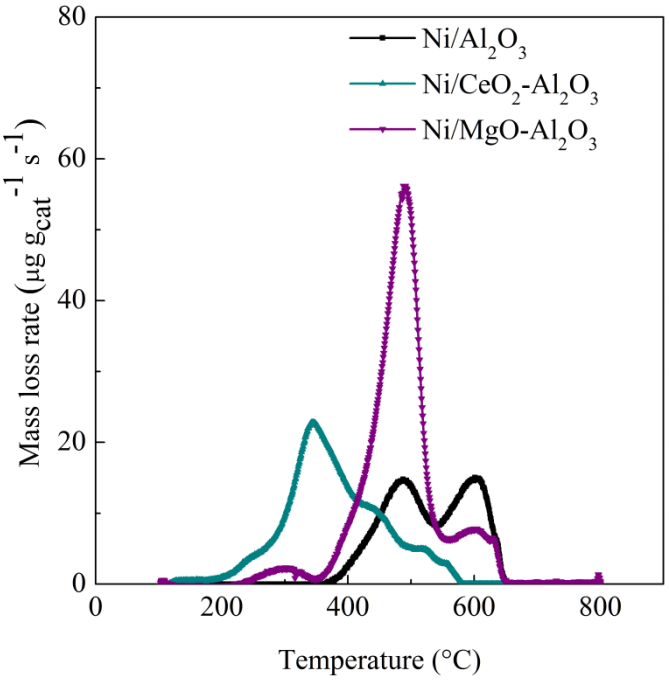

477

478 Figure 7. TPO profiles of the coke deposited on the different catalysts.

479 Figures 8 and 9 show SEM and TEM images, respectively, for Ni/Al_2O_3 (a), Ni/CeO_2-
480 Al_2O_3 (b) and $Ni/MgO\text{-}Al_2O_3$ (c) deactivated catalyst. As observed, none of the
481 catalysts contains filamentous coke; that is, although the coke undergoes graphitization,
482 filaments are not formed, and therefore it is mainly amorphous. Furthermore, the higher
483 Ni particles observed for $Ni/CeO_2\text{-}Al_2O_3$ catalyst by TEM technique are evidence of a
484 slight sintering of this catalyst.

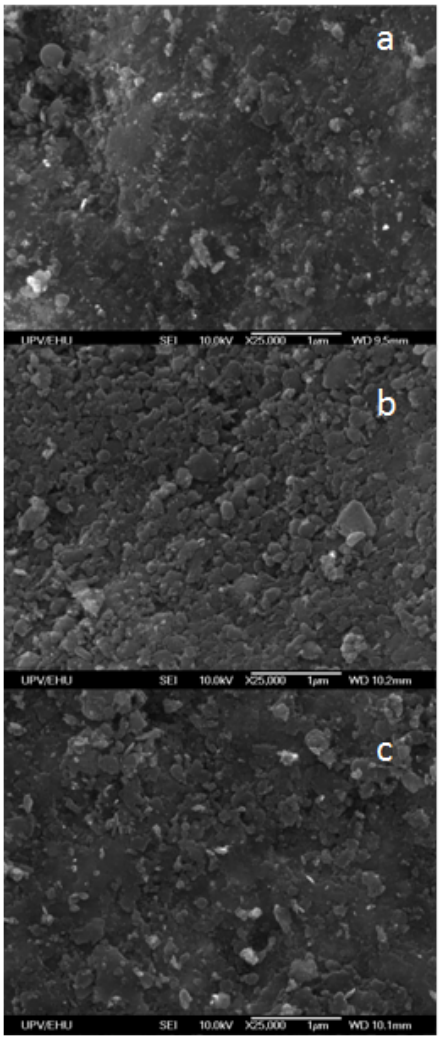

Figure 8. SEM images of deactivated Ni/Al_2O_3 (a), Ni/CeO_2-Al_2O_3 (b) and Ni/MgO-Al_2O_3 (c) catalysts.

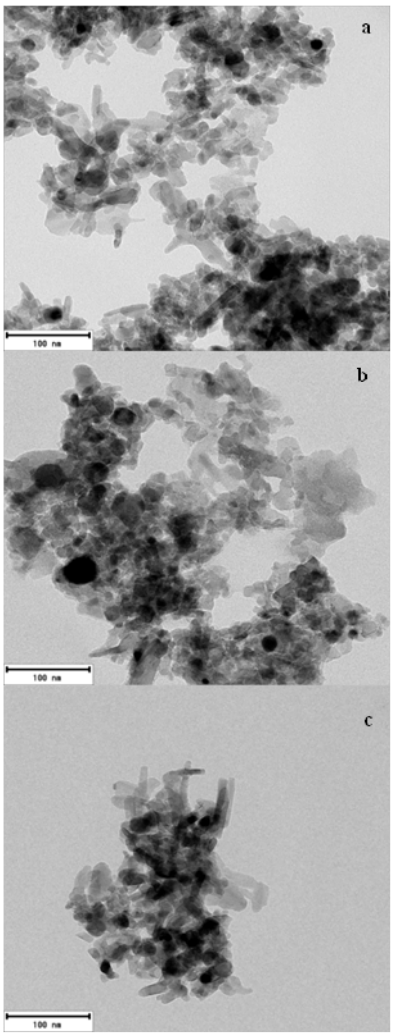

Figure 9. TEM images of deactivated Ni/Al_2O_3 (a), Ni/CeO_2-Al_2O_3 (b) and Ni/MgO-Al_2O_3 (c) catalysts.

TPO-FTIR technique has been used in order to acquire a deeper knowledge about the effect the promoter has on the nature of the coke deposited on each catalyst. Figure 10 shows the evolution of FTIR bands of the different functional groups throughout combustion. According to the literature, the assignment of the FTIR bands in the coke analysis to the functional groups is as follows [77-79]: 880 cm^{-1} to -COOH δ deformation vibration; 1050 cm^{-1} and 1110 cm^{-1} to the stretching vibration of C-O bonds or oxides on the support; 1260 cm^{-1} to the stretching vibration of C-O bonds in alcohols, ethers or related compounds, and/or the stretching asymmetric vibrational

mode of C-O-C bonds; 1385 cm^{-1} to C-H in aliphatics; 1450 cm^{-1} to bending vibrations in $–CH_2$ and $–CH_3$ aliphatic groups and/or symmetric stretching vibrations of O=C-O bonds in acetate groups; 1505 cm^{-1} to symmetric stretching vibrations of O=C-O bonds in carbonate groups and/or C=C bonds in slightly condensed aromatics; 1580 cm^{-1} to C=C in polycondensed aromatics or asymmetric stretching vibrations of O=C-O bonds in acetate groups; 1650 cm^{-1} to C=C stretching vibrations in cyclic alkenes and/or C=O stretching vibrations in aldehydes and ketones; 2850, 2925 and 2960 cm^{-1} to the stretching vibration of C-H in -CHn aliphatic groups; 3450 cm^{-1} to the stretching vibration of O-H bonds, which correspond to the adsorbed water. The assignment of IR bands to particular species is not straightforward due to the high diversity of functional groups in the coke.

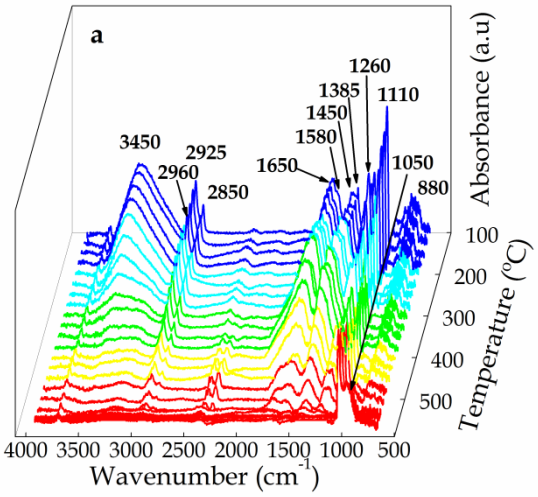

512

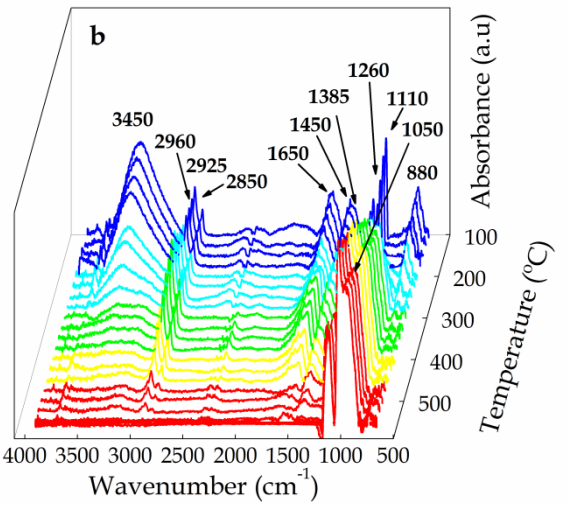

513

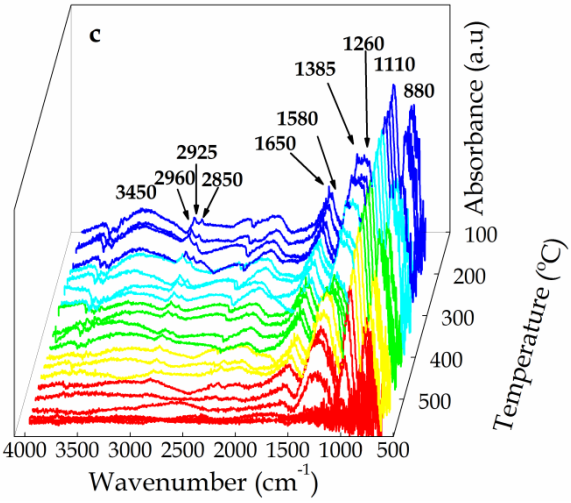

514 Figure 10. Evolution of FTIR bands corresponding to different functional groups with
515 combustion temperature (TPO-FTIR analysis) for the coke deposited on Ni/Al_2O_3 (a),
516 Ni/CeO_2-Al_2O_3 (b) and Ni/MgO-Al_2O_3 (c).

517 As observed, the same FT-IR bands appear in the profiles of the three deactivated
518 catalysts, suggesting that the nature of the coke deposited on the three catalysts is very
519 similar, which corresponds to an oxygenated nature, but their TPO profiles differ
520 depending on the promoter used, with coke combustion temperature being lower for
521 Ni/CeO_2-Al_2O_3 catalyst (Figure 7). In addition, significant features are observed for
522 Ni/CeO_2-Al_2O_3 in the FTIR spectrum, and are summarized as follows: i) 1050 cm^{-1} and
523 1110 cm^{-1} bands associated with the oxides of the support decrease initially, but greatly

524 increase at high temperatures, presumably due to the different oxidation states of this
525 promoter; ii) 3450 cm^{-1} band intensity is very high compared to the other catalysts,
526 which is evidence of a large amount of water adsorbed on this catalyst. Both
527 characteristics of Ni/CeO_2-Al_2O_3 catalyst (its redox properties and the higher capacity
528 for water adsorption) lead to a higher stability, since they minimize coke deposition and
529 enhance precursor gasification [45, 64].

530 **4. Conclusions**

531 Biomass fast pyrolysis in a conical spouted bed reactor and in-line steam reforming of
532 the volatiles formed in a fluidized bed reactor is a highly suitable strategy for H_2
533 production. However, the type of promoter used significantly affects catalyst stability.
534 Thus, Ni/MgO-Al_2O_3 is slightly less stable than Ni/Al_2O_3 catalyst, presumably due to
535 the formation of $MgAl_2O_4$ spinel and the difficulties for reducing the Ni interacting with
536 this spinel. Nevertheless, CeO_2 addition as promoter improves considerably Ni/Al_2O_3
537 catalyst stability, maintaining 60 % conversion once 200 min operation has elapsed,
538 which is related to CeO_2 redox properties, as they increase oxygen availability on the
539 surface, as well as water adsorption capacity, which enhance coke precursor gasification
540 and attenuate catalyst deactivation. Besides, the presence of $CeAlO_3$ spinel also favours
541 coke precursor gasification, and therefore improves catalyst stability.

542 Moreover, although sintering effect is observed for Ni/CeO_2-Al_2O_3 catalyst, which may
543 contribute to catalyst decay, deactivation is mainly associated with the coke deposited
544 on the catalyst, which decreases the BET surface area, pore volume and pore diameter,
545 and therefore partially blocks the support pores. Besides, the coke deposited is not
546 evolved coke and its combustion is catalysed by the metals on the catalyst, and therefore
547 occurs at low temperatures (below 400 ºC). The slower evolution of the coke deposited
548 towards more graphitic coke is attributed to the capability of CeO_2 for coke gasification.

549 Whenever MgO is added to Al_2O_3 support, although the evolution of coke to more
550 graphitic structures is attenuated, higher coke deposition rates are attained, which lead
551 to faster catalyst deactivation.

552 **Acknowledgments**

553 This work was carried out with financial support from the Ministry of Economy and
554 Competitiveness of the Spanish Government (CTQ2016-75535-R (AEI/FEDER, UE),
555 CTQ-2015-69436-R (MINECO/FEDER, UE) and RTI2018-101678-B-I00
556 (MCIU/AEI/FEDER, UE)), the European Commission (HORIZON H2020-MSCA
557 RISE-2018. Contract No. 823745) and the Basque Government (IT1218-19).

558

559

References

[1] Q. Liu, S.C. Chmely, N. Abdoulmoumine, Biomass treatment strategies for thermochemical conversion, Energy Fuels 31 (2017) 3525-3536. https://doi.org/10.1021/acs.energyfuels.7b00258.

[2] N.L. Panwar, R. Kothari, V.V. Tyagi, Thermo chemical conversion of biomass – Eco friendly energy routes, Renewable Sustainable Energy Rev. 16 (2012) 1801-1816. https://doi.org/10.1016/j.rser.2012.01.024.

[3] A. Arregi, G. Lopez, M. Amutio, M. Artetxe, I. Barbarias, J. Bilbao, M. Olazar, Role of operating conditions in the catalyst deactivation in the in-line steam reforming of volatiles from biomass fast pyrolysis, Fuel 216 (2018) 233-244. https://doi.org/10.1016/j.fuel.2017.12.002.

[4] B. Valle, A. Remiro, N. García-Gómez, A.G. Gayubo, J. Bilbao, Recent research progress on bio-oil conversion into bio-fuels and raw chemicals: a review, J. Chem. Technol. Biotechnol. 94 (2019) 670-689. https://doi.org/10.1002/jctb.5758.

[5] A.V. Bridgwater, Review of fast pyrolysis of biomass and product upgrading, Biomass Bioenergy 38 (2012) 68-94. https://doi.org/10.1016/j.biombioe.2011.01.048.

[6] G. Perkins, T. Bhaskar, M. Konarova, Process development status of fast pyrolysis technologies for the manufacture of renewable transport fuels from biomass, Renewable Sustainable Energy Rev. 90 (2018) 292-315. https://doi.org/10.1016/j.rser.2018.03.048.

[7] S. Zarnegar, A review on catalytic-pyrolysis of coal and biomass for value-added fuel and chemicals, Energy Sources Part A 40 (2018) 1427-1433. https://doi.org/10.1080/15567036.2018.1472680.

[8] J. Alvarez, M. Amutio, G. Lopez, I. Barbarias, J. Bilbao, M. Olazar, Sewage sludge valorization by flash pyrolysis in a conical spouted bed reactor, Chem. Eng. J. 273 (2015) 173-183. https://doi.org/10.1016/j.cej.2015.03.047.

[9] A. Molino, S. Chianese, D. Musmarra, Biomass gasification technology: The state of the art overview, J. Energy Chem. 25 (2016) 10-25. https://doi.org/10.1016/j.jechem.2015.11.005.

[10] I.L. Motta, N.T. Miranda, R. Maciel Filho, M.R. Wolf Maciel, Biomass gasification in fluidized beds: A review of biomass moisture content and operating pressure effects, Renewable Sustainable Energy Rev. 94 (2018) 998-1023. https://doi.org/10.1016/j.rser.2018.06.042.

[11] M. Cortazar, J. Alvarez, G. Lopez, M. Amutio, L. Santamaria, J. Bilbao, M. Olazar, Role of temperature on gasification performance and tar composition in a fountain enhanced conical spouted bed reactor, Energy Convers. Manage. 171 (2018) 1589-1597. https://doi.org/10.1016/j.enconman.2018.06.071.

[12] H. Balat, E. Kirtay, Hydrogen from biomass - Present scenario and future prospects, Int. J. Hydrogen Energy 35 (2010) 7416-7426. https://doi.org/10.1016/j.ijhydene.2010.04.137

[13] W. Nabgan, T.A. Tuan Abdullah, R. Mat, B. Nabgan, Y. Gambo, M. Ibrahim, A. Ahmad, A.A. Jalil, S. Triwahyono, I. Saeh, Renewable hydrogen production from bio-oil derivative via catalytic steam reforming: An overview, Renewable Sustainable Energy Rev. 79 (2017) 347-357. https://doi.org/10.1016/j.rser.2017.05.069.

[14] C. Pfeifer, S. Koppatz, H. Hofbauer, Steam gasification of various feedstocks at a dual fluidised bed gasifier: Impacts of operation conditions and bed materials, Biomass Convers. Biorefinery 1 (2011) 39-53. https://doi.org/10.1007/s13399-011-0007-1.

[15] P. Parthasarathy, K.S. Narayanan, Hydrogen production from steam gasification of biomass: Influence of process parameters on hydrogen yield - A review, Renewable Energy 66 (2014) 570-579. https://doi.org/10.1016/j.renene.2013.12.025.

[16] A. Erkiaga, G. Lopez, M. Amutio, J. Bilbao, M. Olazar, Influence of operating conditions on the steam gasification of biomass in a conical spouted bed reactor, Chem. Eng. J. 237 (2014) 259-267. https://doi.org/10.1016/j.cej.2013.10.018.

[17] J. Remón, F. Broust, G. Volle, L. García, J. Arauzo, Hydrogen production from pine and poplar bio-oils by catalytic steam reforming. Influence of the bio-oil composition on the process, Int. J. Hydrogen Energy 40 (2015) 5593-5608. https://doi.org/10.1016/j.ijhydene.2015.02.117.

[18] J. Chen, J. Sun, Y. Wang, Catalysts for Steam Reforming of Bio-oil: A Review, Ind. Eng. Chem. Res. 56 (2017) 4627-4637. https://doi.org/10.1021/acs.iecr.7b00600.

[19] B. Valle, B. Aramburu, M. Olazar, J. Bilbao, A.G. Gayubo, Steam reforming of raw bio-oil over Ni/La_2O_3-αAl_2O_3: Influence of temperature on product yields and catalyst deactivation, Fuel 216 (2018) 463-474. https://doi.org/10.1016/j.fuel.2017.11.149.

[20] F. Seyedeyn Azad, J. Abedi, E. Salehi, T. Harding, Production of hydrogen via steam reforming of bio-oil over Ni-based catalysts: Effect of support, Chem. Eng. J. 180 (2012) 145-150. https://doi.org/10.1016/j.cej.2011.11.027.

[21] A. Arregi, G. Lopez, M. Amutio, I. Barbarias, J. Bilbao, M. Olazar, Hydrogen production from biomass by continuous fast pyrolysis and in-line steam reforming, RSC Adv. 6 (2016) 25975-25985. https://doi.org/10.1039/c6ra01657j.

[22] Z. Ma, S. Zhang, D. Xie, Y. Yan, A novel integrated process for hydrogen production from biomass, Int. J. Hydrogen Energy 39 (2014) 1274-1279. https://doi.org/10.1016/j.ijhydene.2013.10.146.

[23] Y. Liu, H. Yu, J. Liu, D. Chen, Catalytic characteristics of innovative Ni/slag catalysts for syngas production and tar removal from biomass pyrolysis, I Int. J. Hydrogen Energy (2019). https://doi.org/10.1016/j.ijhydene.2019.03.024.

[24] I. Barbarias, G. Lopez, J. Alvarez, M. Artetxe, A. Arregi, J. Bilbao, M. Olazar, A sequential process for hydrogen production based on continuous HDPE fast pyrolysis and in-line steam reforming, Chem. Eng. J. 296 (2016) 191-198. https://doi.org/10.1016/j.cej.2016.03.091.

[25] C. Li, D. Hirabayashi, K. Suzuki, Development of new nickel based catalyst for biomass tar steam reforming producing H_2-rich syngas, Fuel Process. Technol. 90 (2009) 790-796. https://doi.org/10.1016/j.fuproc.2009.02.007.

[26] N. Rakesh, S. Dasappa, A critical assessment of tar generated during biomass gasification - Formation, evaluation, issues and mitigation strategies, Renewable Sustainable Energy Rev. 91 (2018) 1045-1064. https://doi.org/10.1016/j.rser.2018.04.017.

[27] F.L. Chan, A. Tanksale, Review of recent developments in Ni-based catalysts for biomass gasification, Renewable Sustainable Energy Rev. 38 (2014) 428-438. https://doi.org/10.1016/j.rser.2014.06.011.

[28] A. Kumar, J.P. Chakraborty, R. Singh, Bio-oil: the future of hydrogen generation, Biofuels 8 (2017) 663-674. https://doi.org/10.1080/17597269.2016.1141276.

[29] E.C. Vagia, A.A. Lemonidou, Investigations on the properties of ceria–zirconia-supported Ni and Rh catalysts and their performance in acetic acid steam reforming, J. Catal. 269 (2010) 388-396. https://doi.org/10.1016/j.jcat.2009.11.024.

[30] Y. Khani, Z. Shariatinia, F. Bahadoran, High catalytic activity and stability of ZnLaAlO4 supported Ni, Pt and Ru nanocatalysts applied in the dry, steam and combined dry-steam reforming of methane, Chem. Eng. J. 299 (2016) 353-366https://doi.org/10.1016/j.cej.2016.04.108.

[31] M.M. Yung, W.S. Jablonski, K.A. Magrini-Bair, Review of catalytic conditioning of biomass-derived syngas, Energy Fuels 23 (2009) 1874-1887.

[32] F.G.E. Nogueira, P.G.M. Assaf, H.W.P. Carvalho, E.M. Assaf, Catalytic steam reforming of acetic acid as a model compound of bio-oil, Appl. Catal., B 160 (2014) 188-199https://doi.org/10.1016/j.apcatb.2014.05.024.

[33] C. Montero, A. Ochoa, P. Castaño, J. Bilbao, A.G. Gayubo, Monitoring Ni0 and coke evolution during the deactivation of a $Ni/La_2O_3–\alpha Al_2O_3$ catalyst in ethanol steam reforming in a fluidized bed, J. Catal. 331 (2015) 181-192. http://dx.doi.org/10.1016/j.jcat.2015.08.005.

[34] L. Santamaria, G. Lopez, A. Arregi, M. Amutio, M. Artetxe, J. Bilbao, M. Olazar, Stability of different Ni supported catalysts in the in-line steam reforming of biomass fast pyrolysis volatiles, Appl. Catal., B 242 (2019) 109-120. https://doi.org/10.1016/j.apcatb.2018.09.081.

[35] R. Trane, S. Dahl, M.S. Skjøth-Rasmussen, A.D. Jensen, Catalytic steam reforming of bio-oil, Int. J. Hydrogen Energy 37 (2012) 6447-6472. https://doi.org/10.1016/j.ijhydene.2012.01.023.

673 [36] N.D. Charisiou, K.N. Papageridis, L. Tzounis, V. Sebastian, S.J. Hinder, M.A.
674 Baker, M. AlKetbi, K. Polychronopoulou, M.A. Goula, Ni supported on CaO-MgO-
675 Al_2O_3 as a highly selective and stable catalyst for H_2 production via the glycerol steam
676 reforming reaction, Int. J. Hydrogen Energy 44 (2019) 256-273.
677 https://doi.org/10.1016/j.ijhydene.2018.02.165.

678 [37] H.D. Demsash, K.V.K. Kondamudi, S. Upadhyayula, R. Mohan, Ruthenium doped
679 nickel-alumina-ceria catalyst in glycerol steam reforming, Fuel Process. Technol. 169
680 (2018) 150-156. https://doi.org/10.1016/j.fuproc.2017.09.017.

681 [38] N.D. Charisiou, G. Siakavelas, K.N. Papageridis, A. Baklavaridis, L. Tzounis, K.
682 Polychronopoulou, M.A. Goula, Hydrogen production via the glycerol steam reforming
683 reaction over nickel supported on alumina and lanthana-alumina catalysts, Int. J.
684 Hydrogen Energy 42 (2017) 13039-13060.
685 https://doi.org/10.1016/j.ijhydene.2017.04.048.

686 [39] H. Liu, X. Zou, X. Wang, X. Lu, W. Ding, Effect of CeO_2 addition on Ni/Al_2O_3
687 catalysts for methanation of carbon dioxide with hydrogen, J. Nat. Gas Chem. 21 (2012)
688 703-707. https://doi.org/10.1016/S1003-9953(11)60422-2.

689 [40] R.B. Duarte, M. Nachtegaal, J.M.C. Bueno, J.A. van Bokhoven, Understanding the
690 effect of Sm_2O_3 and CeO_2 promoters on the structure and activity of Rh/Al_2O_3 catalysts
691 in methane steam reforming, J. Catal. 296 (2012) 86-98.
692 https://doi.org/10.1016/j.jcat.2012.09.007.

693 [41] R. Zhang, Y. Wang, R.C. Brown, Steam reforming of tar compounds over
694 Ni/olivine catalysts doped with CeO_2, Energy Convers. Manage. 48 (2007) 68-77.
695 https://doi.org/10.1016/j.enconman.2006.05.001.

696 [42] B. Matas Güell, I.V. Babich, L. Lefferts, K. Seshan, Steam reforming of phenol
697 over Ni-based catalysts – A comparative study, Appl. Catal., B 106 (2011) 280-286.
698 https://doi.org/10.1016/j.apcatb.2011.05.012.

699 [43] W. Chen, G. Zhao, Q. Xue, L. Chen, Y. Lu, High carbon-resistance Ni/CeAlO3-
700 Al2O3 catalyst for CH_4/CO_2 reforming, Appl. Catal., B 136-137 (2013) 260-268.
701 https://doi.org/10.1016/j.apcatb.2013.01.044.

702 [44] K. Polychronopoulou, J.L.G. Fierro, A.M. Efstathiou, The phenol steam reforming
703 reaction over MgO-based supported Rh catalysts, J. Catal. 228 (2004) 417-432.
704 https://doi.org/10.1016/j.jcat.2004.09.016.

705 [45] M.C. Sánchez-Sánchez, R.M. Navarro, J.L.G. Fierro, Ethanol steam reforming
706 over Ni/M_xO_y-Al_2O_3 (M = Ce, La, Zr and Mg) catalysts: Influence of support on the
707 hydrogen production, Int. J. Hydrogen Energy 32 (2007) 1462-1471.
708 https://doi.org/10.1016/j.ijhydene.2006.10.025.

709 [46] L. Santamaria, G. Lopez, A. Arregi, M. Amutio, M. Artetxe, J. Bilbao, M. Olazar,
710 Influence of the support on Ni catalysts performance in the in-line steam reforming of
711 biomass fast pyrolysis derived volatiles, Appl. Catal., B 229 (2018) 105-113.
712 https://doi.org/10.1016/j.apcatb.2018.02.003.

[47] T. Miyazawa, T. Kimura, J. Nishikawa, S. Kado, K. Kunimori, K. Tomishige, Catalytic performance of supported Ni catalysts in partial oxidation and steam reforming of tar derived from the pyrolysis of wood biomass, Catal. Today 115 (2006) 254-262. https://doi.org/10.1016/j.cattod.2006.02.055.

[48] M. Amutio, G. Lopez, R. Aguado, J. Bilbao, M. Olazar, Biomass oxidative flash pyrolysis: Autothermal operation, yields and product properties, Energy Fuels 26 (2012) 1353-1362. https://doi.org/10.1021/ef201662x

[49] J. Alvarez, G. Lopez, M. Amutio, J. Bilbao, M. Olazar, Bio-oil production from rice husk fast pyrolysis in a conical spouted bed reactor, Fuel 128 (2014) 162-169. https://doi.org/10.1016/j.fuel.2014.02.074.

[50] A.R. Fernandez-Akarregi, J. Makibar, G. Lopez, M. Amutio, M. Olazar, Design and operation of a conical spouted bed reactor pilot plant (25 kg/h) for biomass fast pyrolysis, Fuel Process. Technol. 112 (2013) 48-56. https://doi.org/10.1016/j.fuproc.2013.02.022.

[51] J. Alvarez, B. Hooshdaran, M. Cortazar, M. Amutio, G. Lopez, F.B. Freire, M. Haghshenasfard, S.H. Hosseini, M. Olazar, Valorization of citrus wastes by fast pyrolysis in a conical spouted bed reactor, Fuel 224 (2018) 111-120. https://doi.org/10.1016/j.fuel.2018.03.028.

[52] G. Lopez, J. Alvarez, M. Amutio, N.M. Mkhize, B. Danon, P. van der Gryp, J.F. Görgens, J. Bilbao, M. Olazar, Waste truck-tyre processing by flash pyrolysis in a conical spouted bed reactor, Energy Convers. Manage. 142 (2017) 523-532. https://doi.org/10.1016/j.enconman.2017.03.051.

[53] G. Lopez, M. Olazar, R. Aguado, G. Elordi, M. Amutio, M. Artetxe, J. Bilbao, Vacuum pyrolysis of waste tires by continuously feeding into a conical spouted bed reactor, Ind. Eng. Chem. Res. 49 (2010) 8990-8997. https://doi.org/10.1021/ie1000604

[54] J. Alvarez, G. Lopez, M. Amutio, N.M. Mkhize, B. Danon, P. van der Gryp, J.F. Görgens, J. Bilbao, M. Olazar, Evaluation of the properties of tyre pyrolysis oils obtained in a conical spouted bed reactor, Energy 128 (2017) 463-474. https://doi.org/10.1016/j.energy.2017.03.163.

[55] M. Artetxe, G. Lopez, M. Amutio, G. Elordi, M. Olazar, J. Bilbao, Operating conditions for the pyrolysis of poly-(ethylene terephthalate) in a conical spouted-bed reactor, Ind. Eng. Chem. Res. 49 (2010) 2064-2069. https://doi.org/10.1021/ie900557c

[56] G. Elordi, M. Olazar, G. Lopez, M. Artetxe, J. Bilbao, Product yields and compositions in the continuous pyrolysis of high-density polyethylene in a conical spouted bed reactor, Ind. Eng. Chem. Res. 50 (2011) 6650-6659. https://doi.org/10.1021/ie200186m.

[57] G. Lopez, M. Artetxe, M. Amutio, G. Elordi, R. Aguado, M. Olazar, J. Bilbao, Recycling poly-(methyl methacrylate) by pyrolysis in a conical spouted bed reactor, Chem. Eng. Process. Process Intensif. 49 (2010) 1089-1094. https://doi.org/10.1016/j.cep.2010.08.002.

753 [58] M. Amutio, G. Lopez, M. Artetxe, G. Elordi, M. Olazar, J. Bilbao, Influence of
754 temperature on biomass pyrolysis in a conical spouted bed reactor, Resour. Conserv.
755 Recycl. 59 (2012) 23-31. https://doi.org/10.1016/j.resconrec.2011.04.002.

756 [59] A. Erkiaga, G. Lopez, I. Barbarias, M. Artetxe, M. Amutio, J. Bilbao, M. Olazar,
757 HDPE pyrolysis-steam reforming in a tandem spouted bed-fixed bed reactor for H_2
758 production, J. Anal. Appl. Pyrolysis 116 (2015) 34-41.
759 https://doi.org/10.1016/j.jaap.2015.10.010.

760 [60] P. Osorio-Vargas, N.A. Flores-González, R.M. Navarro, J.L.G. Fierro, C.H.
761 Campos, P. Reyes, Improved stability of Ni/Al_2O_3 catalysts by effect of promoters
762 (La_2O_3, CeO_2) for ethanol steam-reforming reaction, Catal. Today 259 (2016) 27-38.
763 https://doi.org/10.1016/j.cattod.2015.04.037.

764 [61] Q. Li, S. Ji, J. Hu, S. Jiang, Catalytic steam reforming of rice straw biomass to
765 hydrogen-rich syngas over Ni-based catalysts, Chinese J. Catal. 34 (2013) 1462-1468.
766 https://doi.org/10.1016/S1872-2067(12)60618-4.

767 [62] R.M. Navarro, R. Guil-Lopez, A.A. Ismail, S.A. Al-Sayari, J.L.G. Fierro, Ni- and
768 PtNi-catalysts supported on Al_2O_3 for acetone steam reforming: Effect of the
769 modification of support with Ce, La and Mg, Catal. Today 242 (2015) 60-70.
770 https://doi.org/10.1016/j.cattod.2014.07.036.

771 [63] D.G. Mustard, C.H. Bartholomew, Determination of metal crystallite size and
772 morphology in supported nickel catalysts, J. Catal. 67 (1981) 186-206.
773 https://doi.org/10.1016/0021-9517(81)90271-2.

774 [64] H.H. Ibrahim, R.O. Idem, Single and mixed oxide-supported nickel catalysts for
775 the catalytic partial oxidation reforming of gasoline, Energy Fuels 22 (2008) 878-891.
776 https://doi.org/10.1021/ef7005904.

777 [65] JCPDS Power Diffraction File, International Centre for Diffraction Data (2003).

778 [66] B. Valle, B. Aramburu, A. Remiro, J. Bilbao, A.G. Gayubo, Effect of
779 calcination/reduction conditions of Ni/La_2O_3-αAl_2O_3 catalyst on its activity and stability
780 for hydrogen production by steam reforming of raw bio-oil/ethanol, Appl. Catal., B 147
781 (2014) 402-410. https://doi.org/10.1016/j.apcatb.2013.09.022.

782 [67] R.M. Navarro, M.C. Álvarez-Galván, F. Rosa, J.L.G. Fierro, Hydrogen production
783 by oxidative reforming of hexadecane over Ni and Pt catalysts supported on Ce/La-
784 doped Al_2O_3, Appl. Catal., A 297 (2006) 60-72.
785 https://doi.org/10.1016/j.apcata.2005.08.036.

786 [68] I. Luisetto, S. Tuti, C. Battocchio, S. Lo Mastro, A. Sodo, Ni/CeO_2–Al_2O_3 catalysts
787 for the dry reforming of methane: The effect of $CeAlO_3$ content and nickel crystallite
788 size on catalytic activity and coke resistance, Appl. Catal., A 500 (2015) 12-22.
789 https://doi.org/10.1016/j.apcata.2015.05.004.

[69] L. Garcia, A. Benedicto, E. Romeo, M.L. Salvador, J. Arauzo, R. Bilbao, Hydrogen production by steam gasification of biomass using Ni-Al coprecipitated catalysts promoted with magnesium, Energy and Fuels 16 (2002) 1222-1230.

[70] M. Tan, X. Wang, X. Wang, X. Zou, W. Ding, X. Lu, Influence of calcination temperature on textural and structural properties, reducibility, and catalytic behavior of mesoporous γ-alumina-supported Ni–Mg oxides by one-pot template-free route, J. Catal. 329 (2015) 151-166. https://doi.org/10.1016/j.jcat.2015.05.011.

[71] Y. Qiu, J. Chen, J. Zhang, Effects of MgO promoter on properties of Ni/Al_2O_3 catalysts for partial oxidation of methane to syngas, J. Fuel Chem. Technol. 34 (2006) 450-455.

[72] Z. Zhang, X. Hu, L. Zhang, Y. Yang, Q. Li, H. Fan, Q. Liu, T. Wei, C. Li, Steam reforming of guaiacol over Ni/Al2O3 and Ni/SBA-15: Impacts of support on catalytic behaviors of nickel and properties of coke, Fuel Process. Technol. 191 (2019) 138-151. https://doi.org/10.1016/j.fuproc.2019.04.001.

[73] N.D. Charisiou, G. Siakavelas, K.N. Papageridis, A. Baklavaridis, L. Tzounis, D.G. Avraam, M.A. Goula, Syngas production via the biogas dry reforming reaction over nickel supported on modified with CeO_2 and/or La_2O_3 alumina catalysts, J. Nat. Gas Sci. Eng. 31 (2016) 164-183. https://doi.org/10.1016/j.jngse.2016.02.021.

[74] A. Arregi, M. Amutio, G. Lopez, J. Bilbao, M. Olazar, Evaluation of thermochemical routes for hydrogen production from biomass: A review, Energy Convers. Manage. 165 (2018) 696-719. https://doi.org/10.1016/j.enconman.2018.03.089.

[75] B. Valle, B. Aramburu, P.L. Benito, J. Bilbao, A.G. Gayubo, Biomass to hydrogen-rich gas via steam reforming of raw bio-oil over Ni/La_2O_3-αAl_2O_3 catalyst: Effect of space-time and steam-to-carbon ratio, Fuel 216 (2018) 445-455. https://doi.org/10.1016/j.fuel.2017.11.151.

[76] F. Bimbela, D. Chen, J. Ruiz, L. García, J. Arauzo, Ni/Al coprecipitated catalysts modified with magnesium and copper for the catalytic steam reforming of model compounds from biomass pyrolysis liquids, Appl. Catal., B 119-120 (2012) 1-12. https://doi.org/10.1016/j.apcatb.2012.02.007.

[77] E. Pretsch, P. Bühlmann, M. Badertscher, Structure determination of organic compounds: Tables of spectral data. Berlin, Heidelberg: Springer; 2009. https://doi.org/10.1007/978-3-540-93810-1.

[78] W. Xu, Z. Liu, A.C. Johnston-Peck, S.D. Senanayake, G. Zhou, D. Stacchiola, E.A. Stach, J.A. Rodriguez, Steam reforming of ethanol on Ni/CeO_2: Reaction pathway and interaction between Ni and the CeO_2 support, ACS Catal. 3 (2013) 975-984. https://doi.org/10.1021/cs4000969.

[79] A. Ochoa, B. Aramburu, B. Valle, D.E. Resasco, J. Bilbao, A.G. Gayubo, P. Castaño, Role of oxygenates and effect of operating conditions in the deactivation of a

Ni supported catalyst during the steam reforming of bio-oil, Green Chem. 19 (2017) 4315-4333. https://doi.org/10.1039/c7gc01432e.

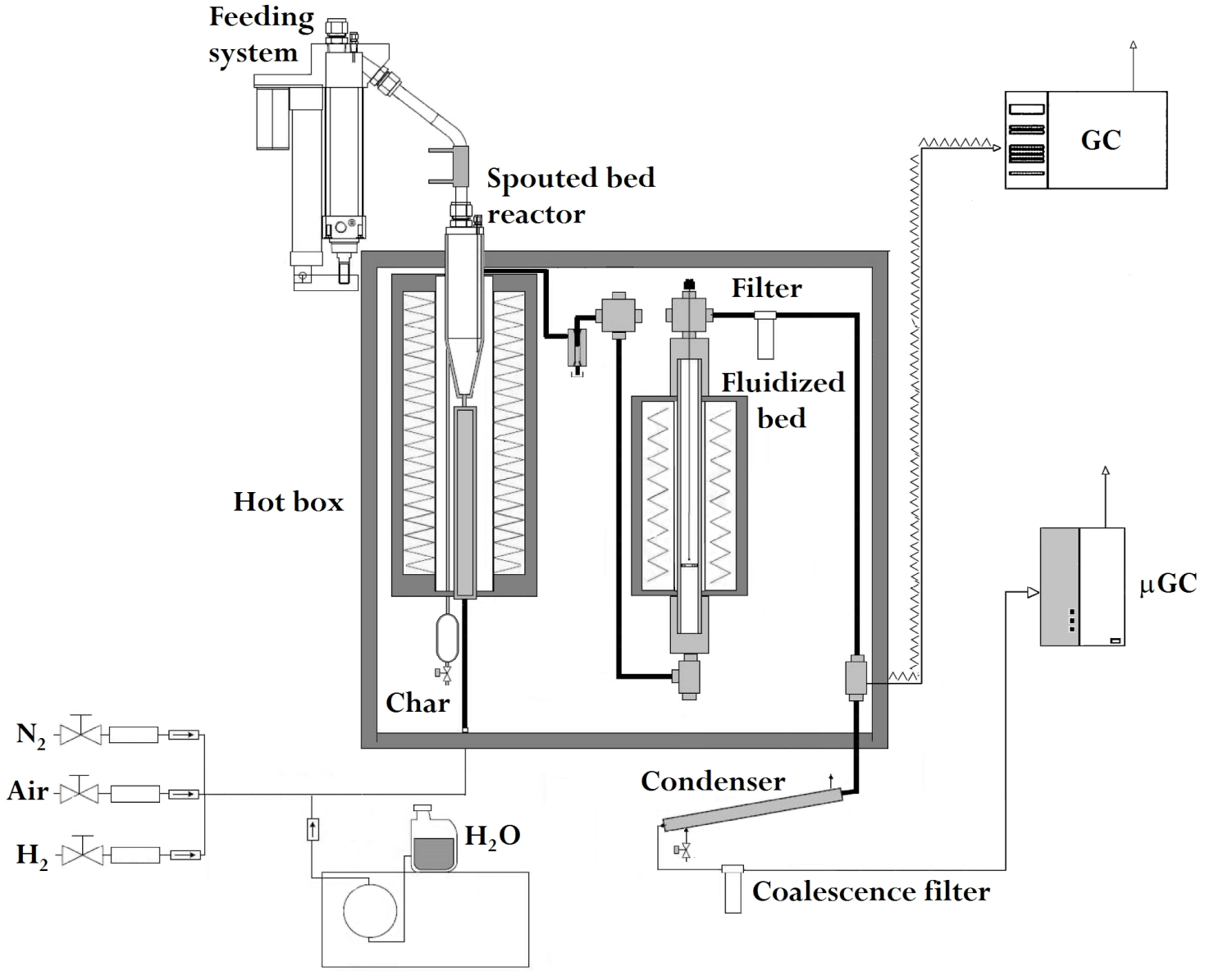
Feeding system
Spouted bed reactor
GC
Filter
Fluidized bed
Hot box
µGC
Char
N_2
Air
H_2
H_2O
Condenser
Coalescence filter

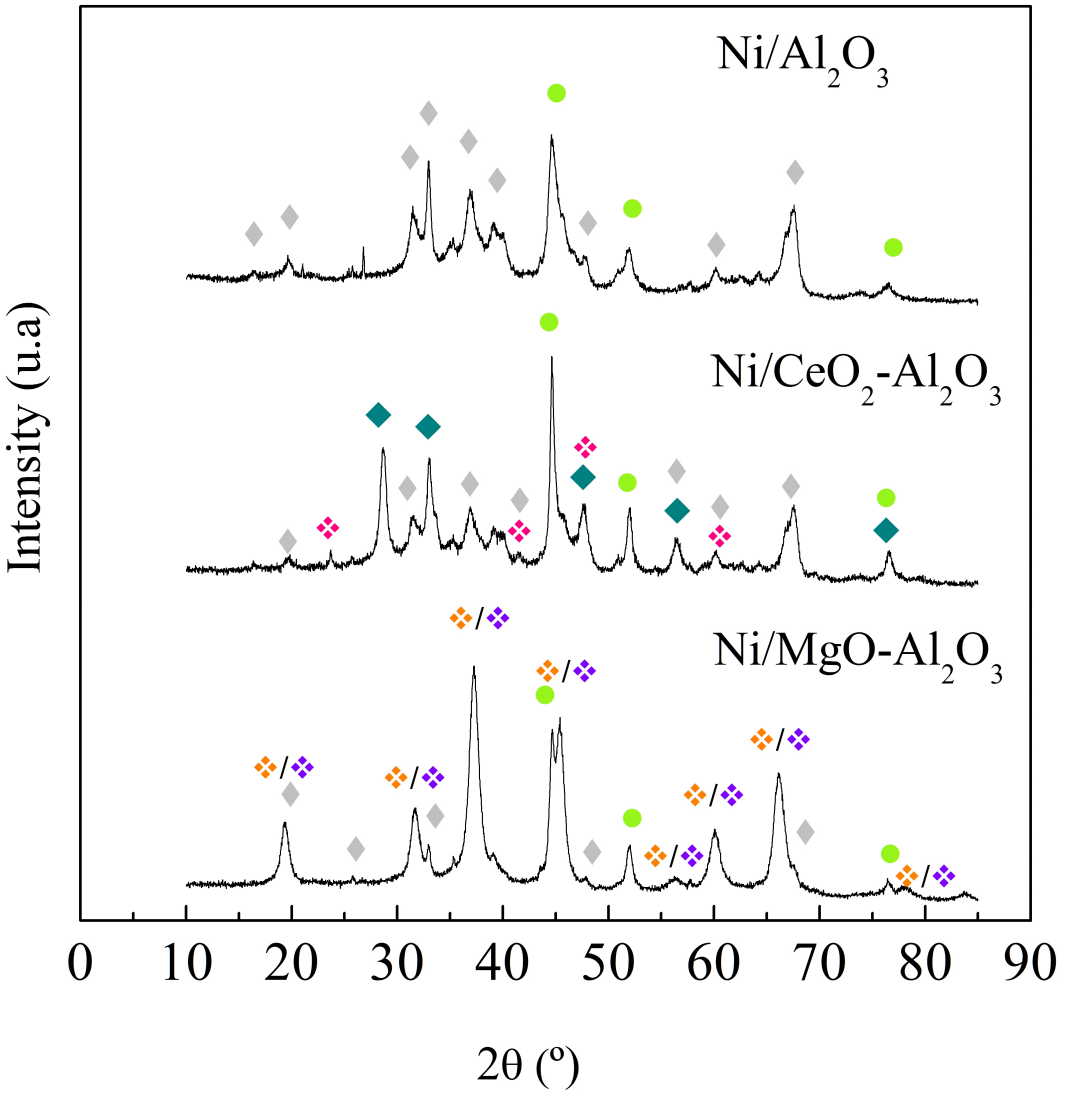
Ni/Al2O3
Ni/CeO2-Al2O3
Ni/MgO-Al2O3
Intensity (u.a)
0
10
20
30
40
50
60
70
80
90
2θ (º)

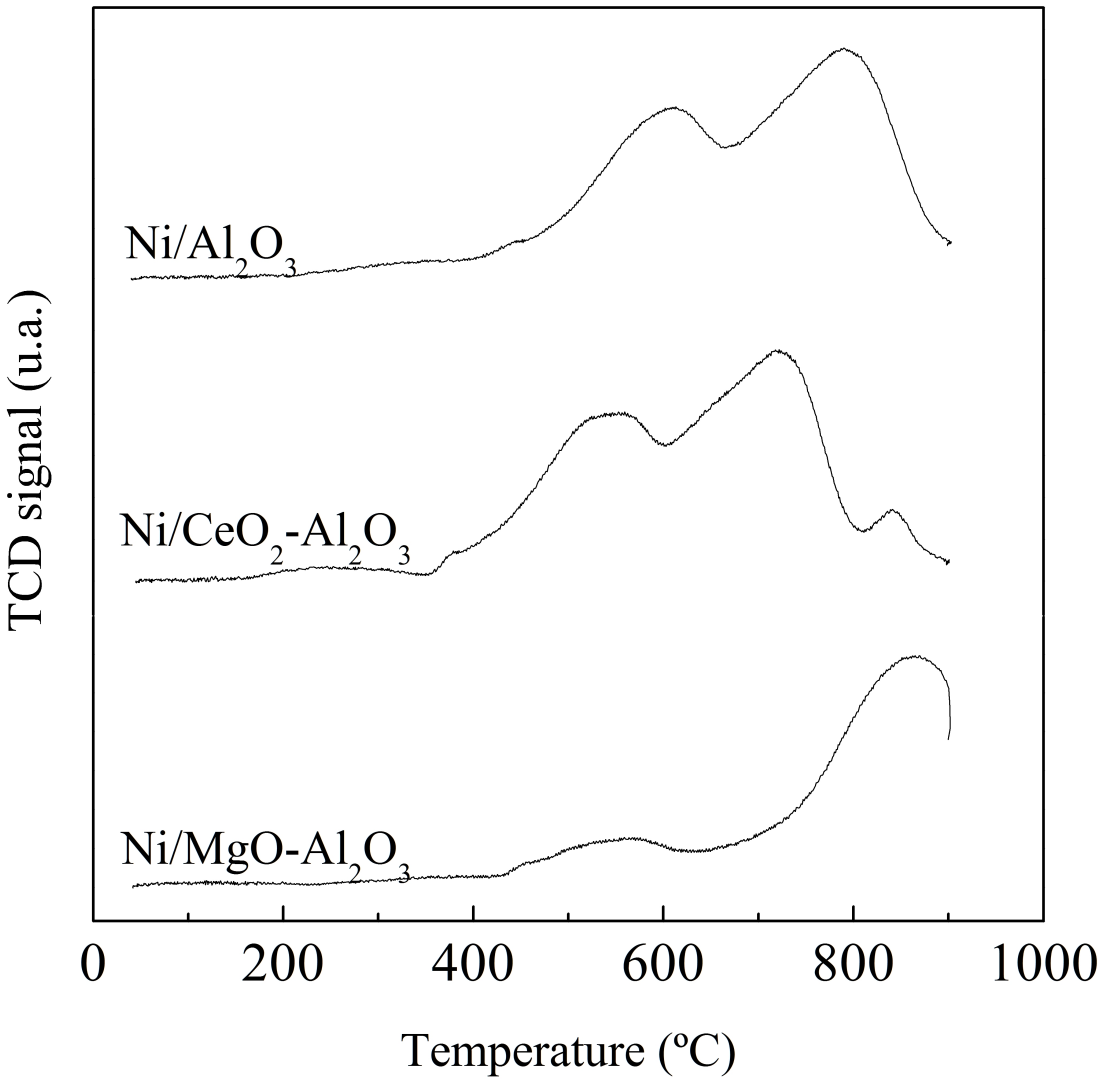
Ni/Al2O3
Ni/CeO2-Al2O3
Ni/MgO-Al2O3
TCD signal (u.a.)
0
200
400
600
800
1000
Temperature (ºC)

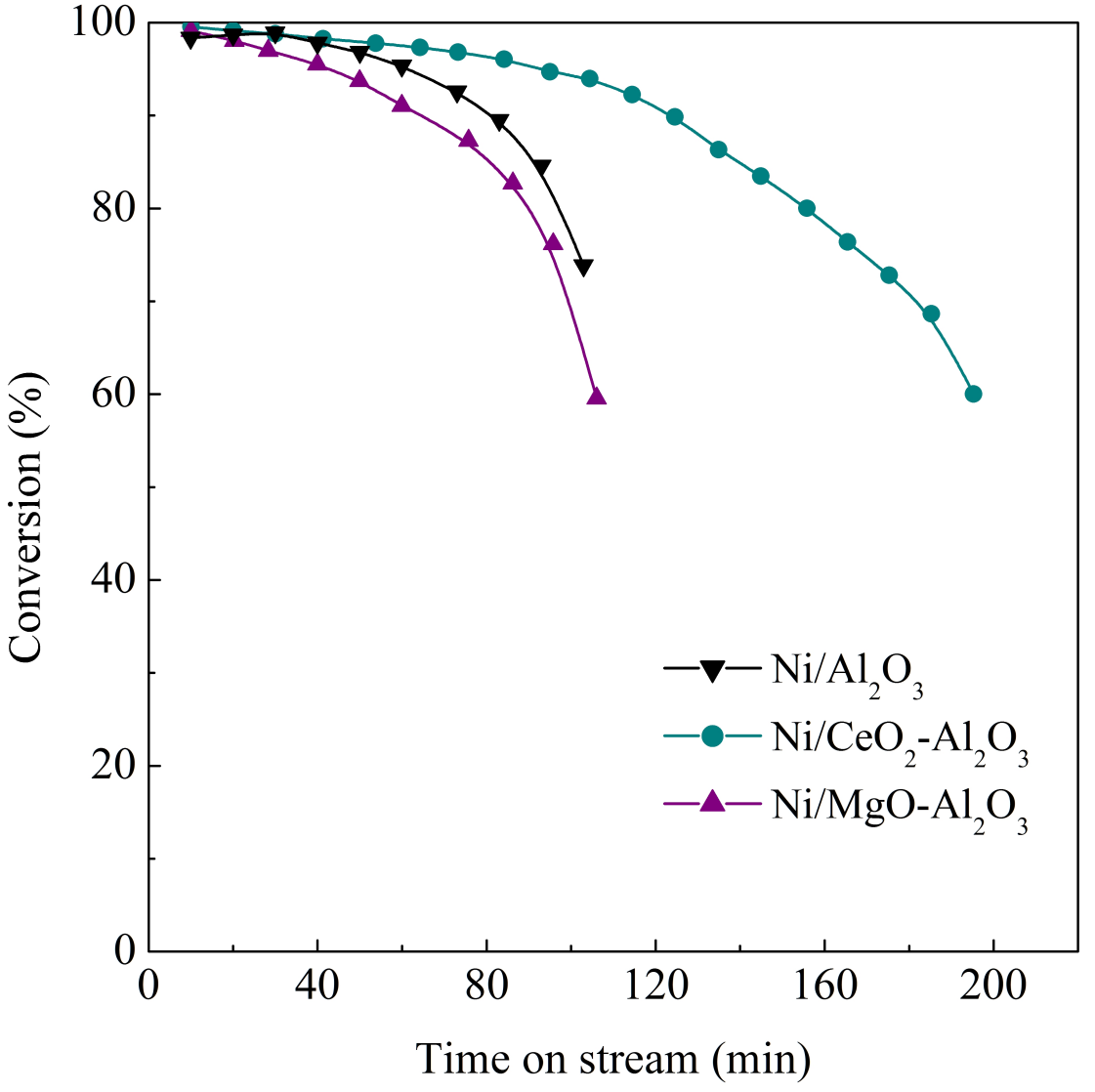
100
80
60
40
20
0
Conversion (%)
0
40
80
120
160
200
Time on stream (min)
Ni/Al2O3
Ni/CeO2-Al2O3
Ni/MgO-Al2O3

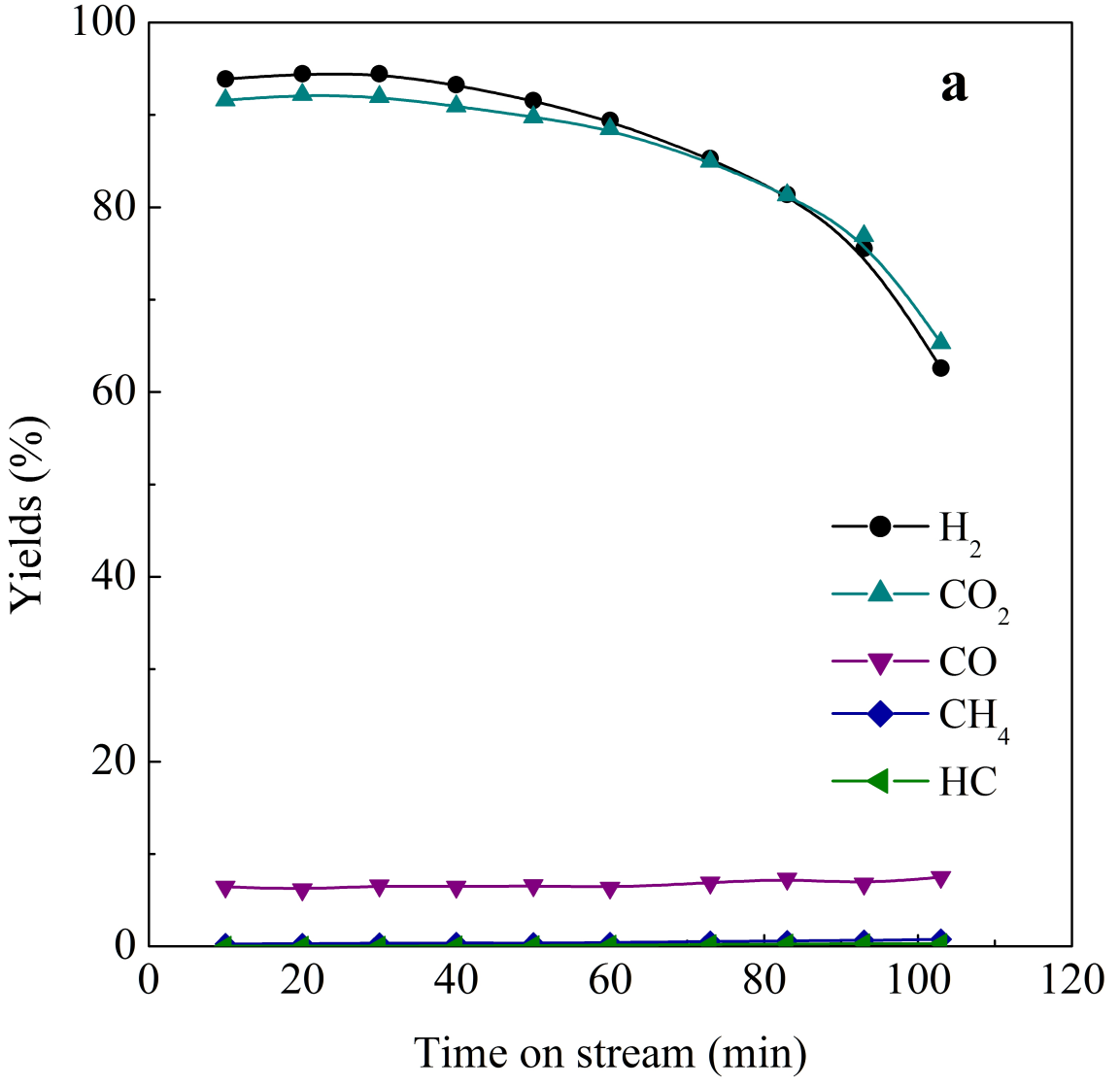
a
Yields (%)
Time on stream (min)
H2
CO2
CO
CH4
HC
0
20
40
60
80
100
120

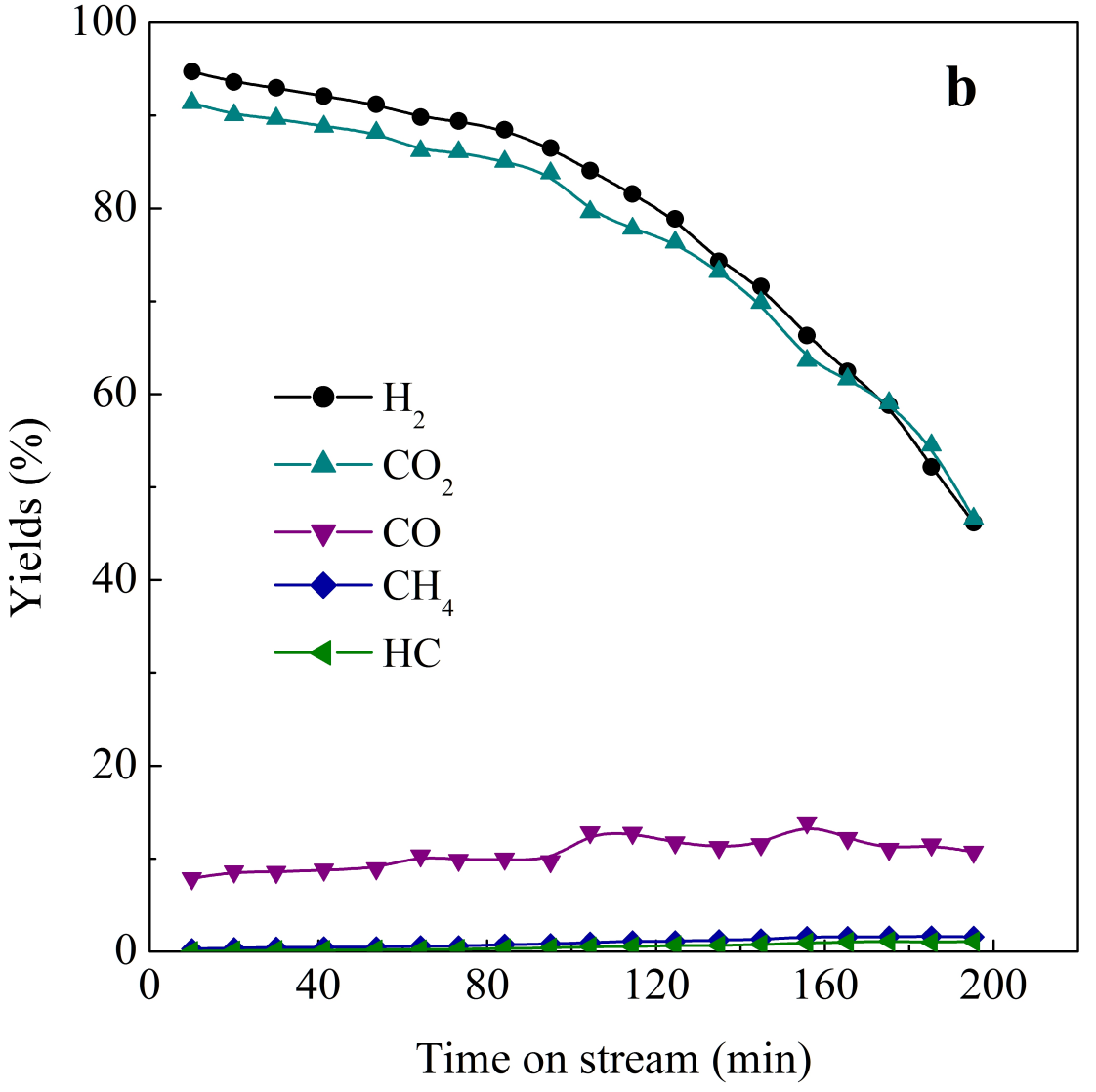
b
100
80
60
40
20
0
Yields (%)
0
40
80
120
160
200
Time on stream (min)
H2
CO2
CO
CH4
HC

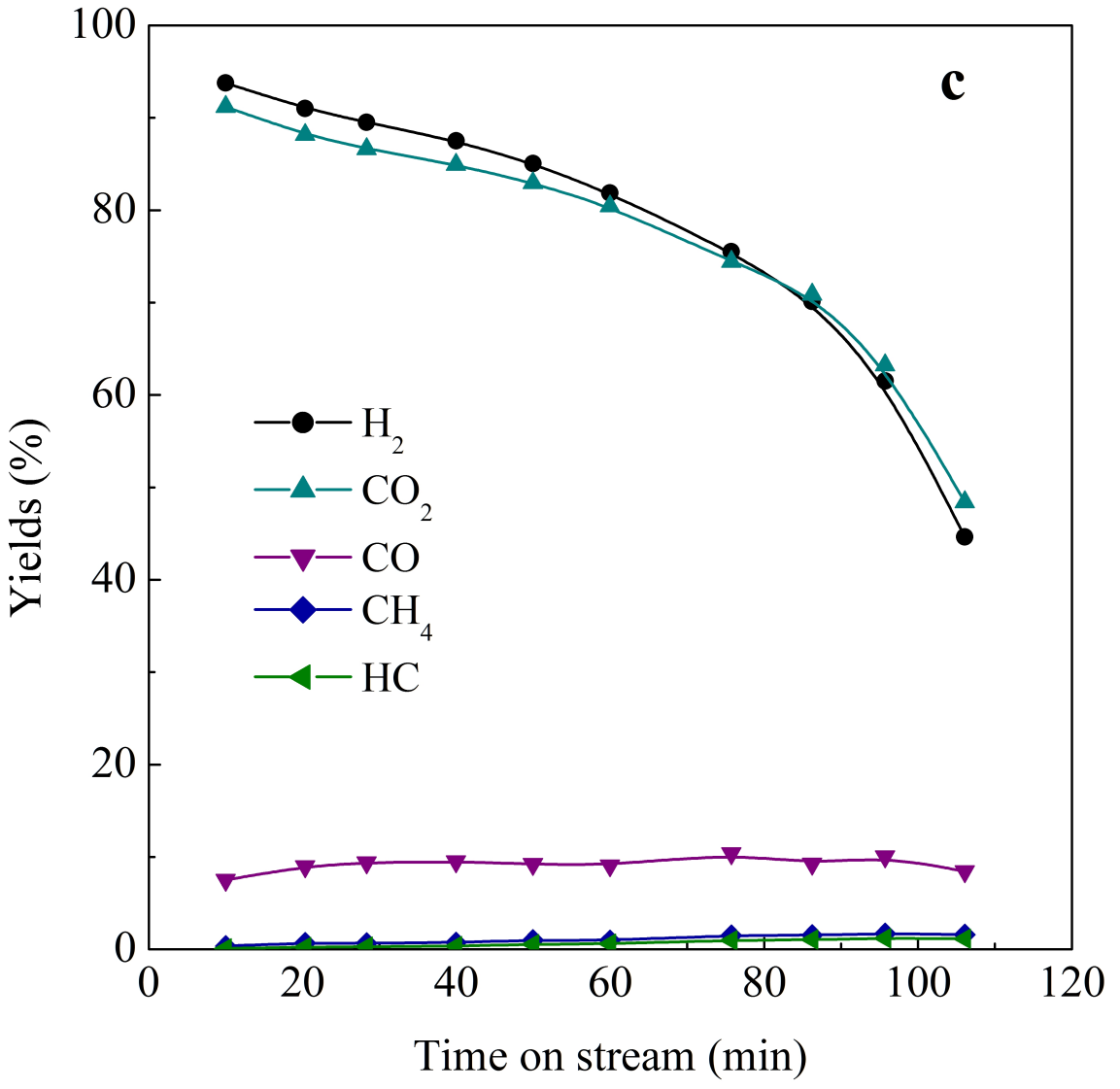
c
Yields (%)
Time on stream (min)
H2
CO2
CO
CH4
HC
0
20
40
60
80
100
120

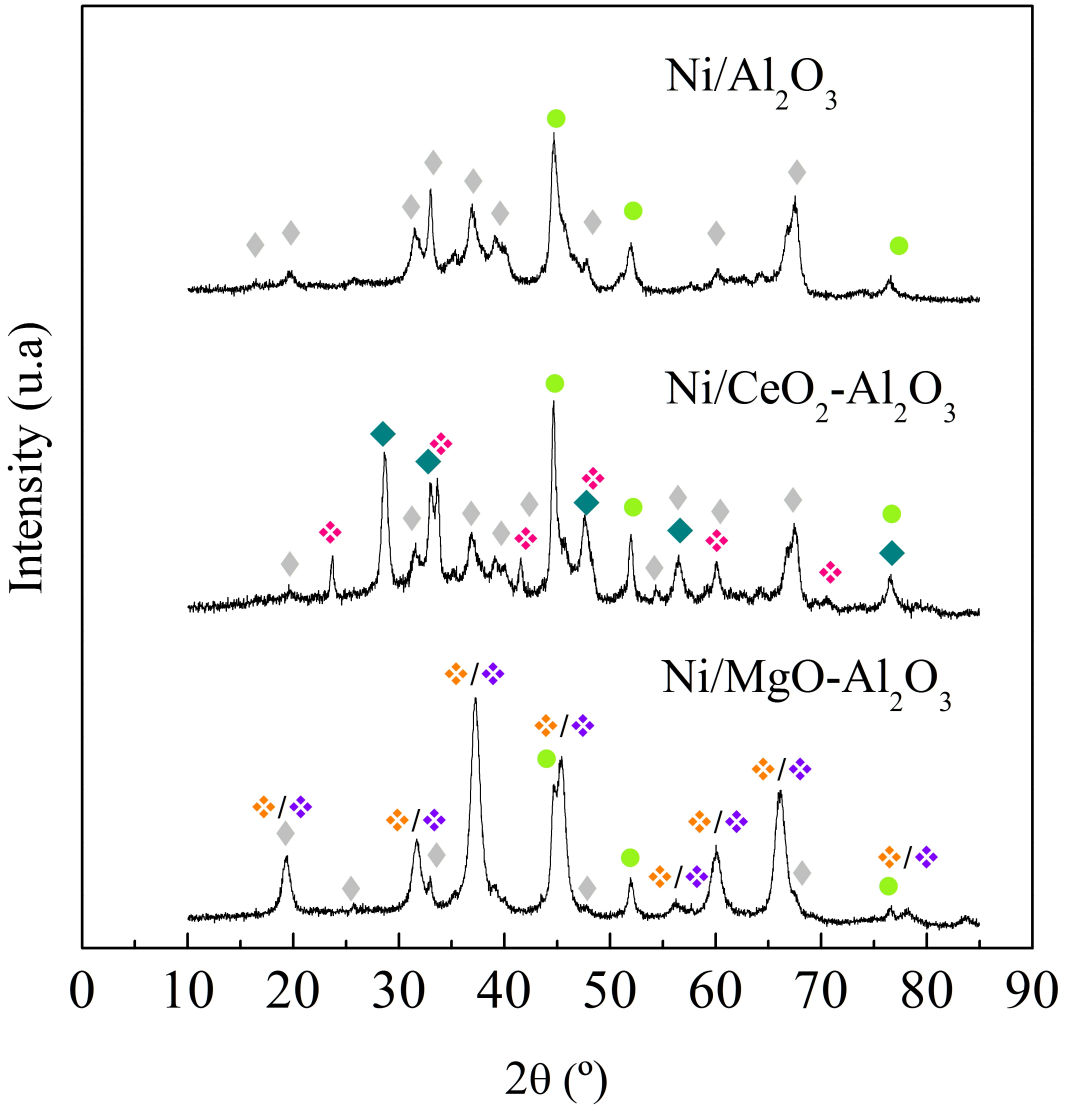
Ni/Al2O3
Ni/CeO2-Al2O3
Ni/MgO-Al2O3
Intensity (u.a)
0
10
20
30
40
50
60
70
80
90
2θ (º)

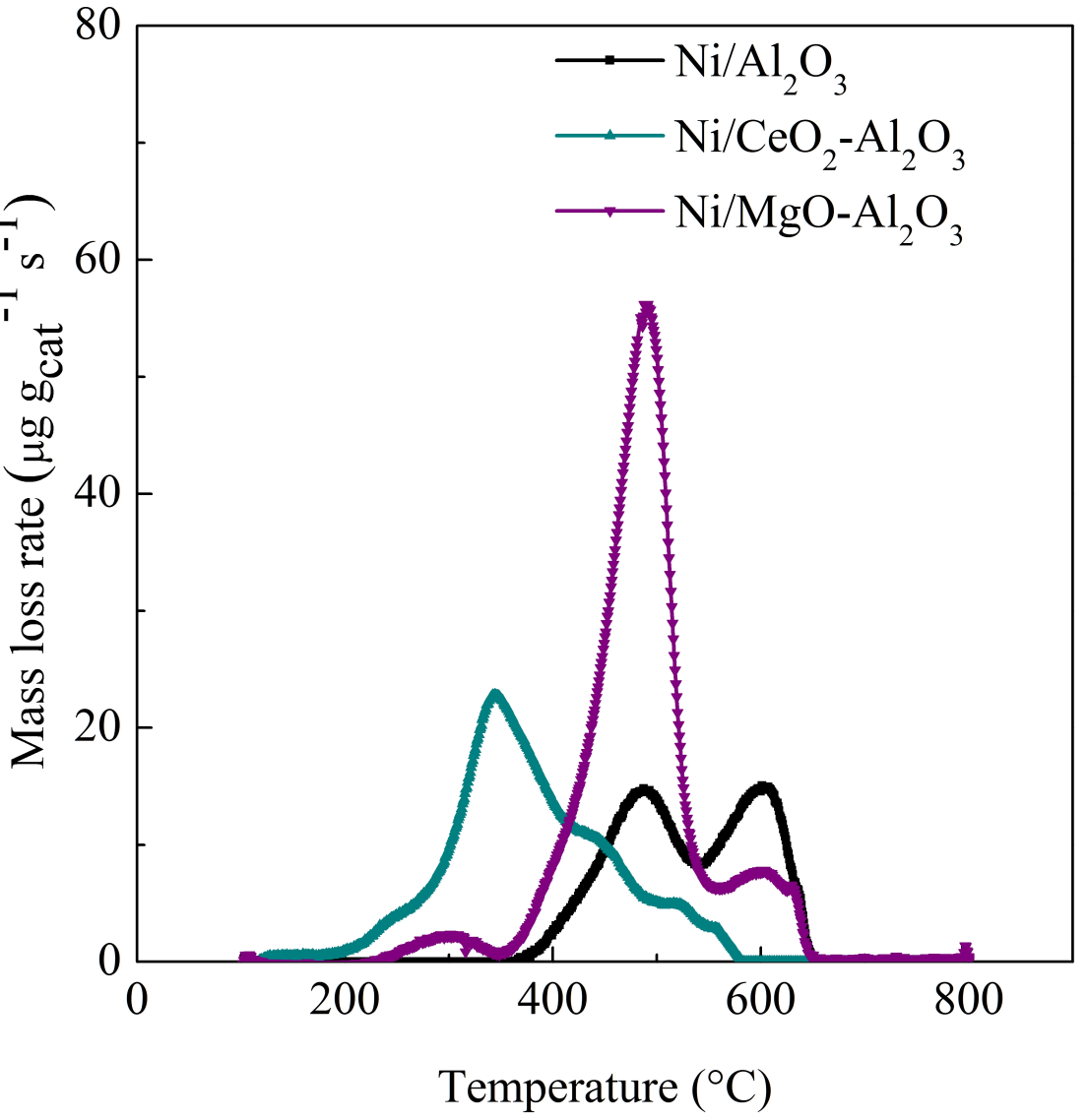
Ni/Al2O3
Ni/CeO2-Al2O3
Ni/MgO-Al2O3
Mass loss rate (μg gcat-1 s-1)
Temperature (°C)
0
20
40
60
80
0
200
400
600
800

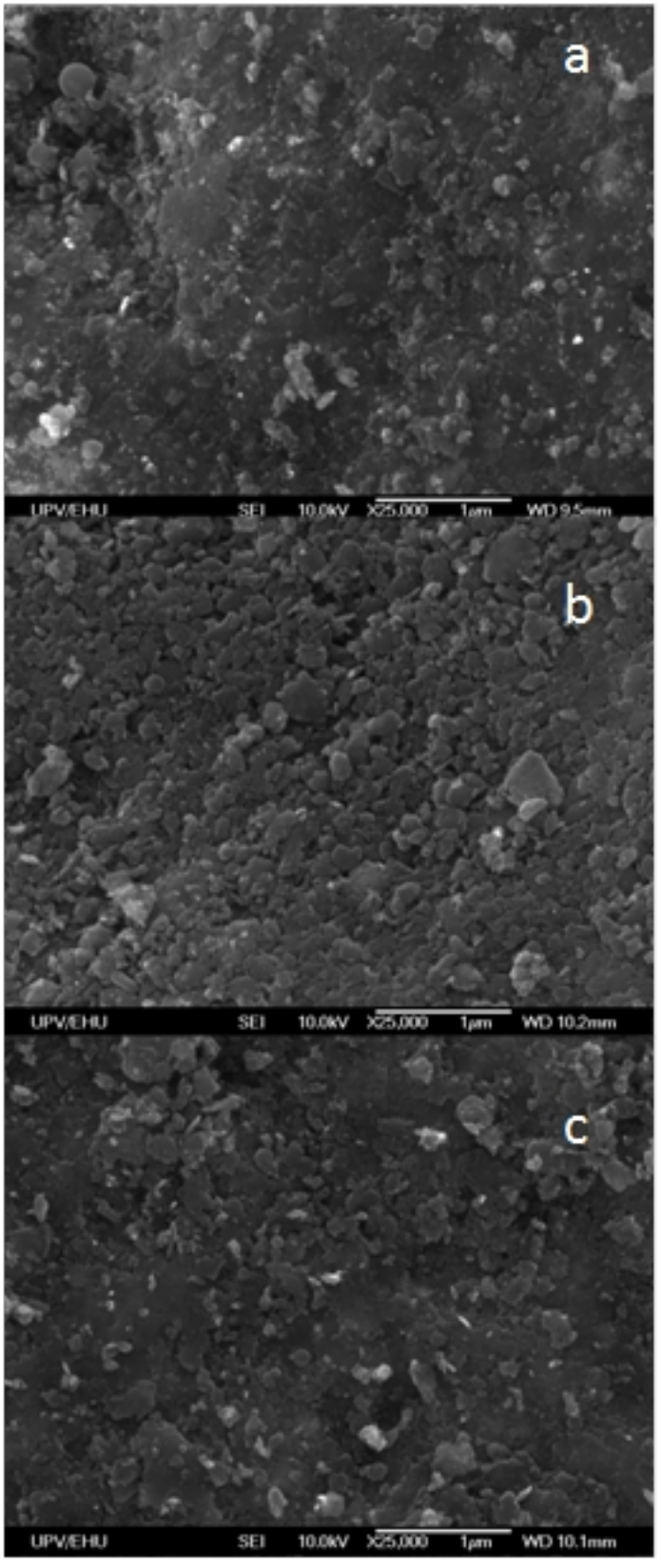
a
UPV/EHU SEI 10.0kV X25,000 1μm WD 9.5mm
b
UPV/EHU SEI 10.0kV X25,000 1μm WD 10.2mm
c
UPV/EHU SEI 10.0kV X25,000 1μm WD 10.1mm

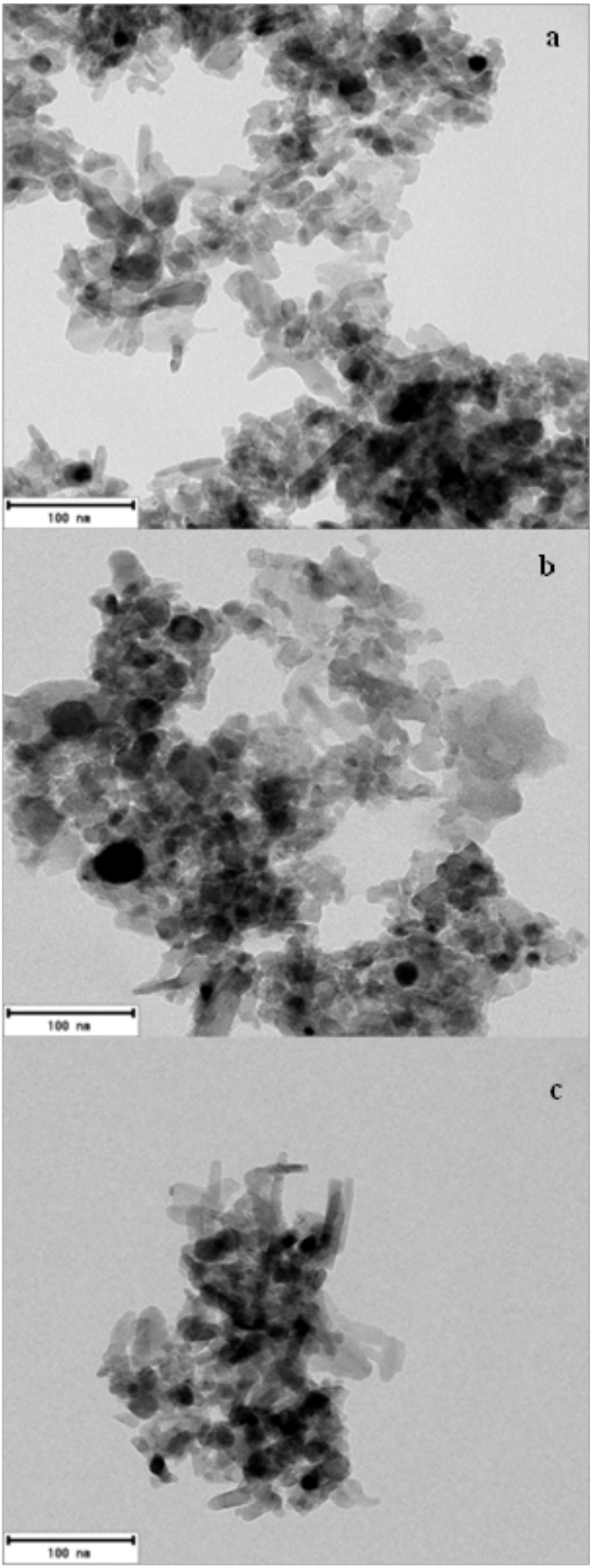
a
100 nm
b
100 nm
c
100 nm

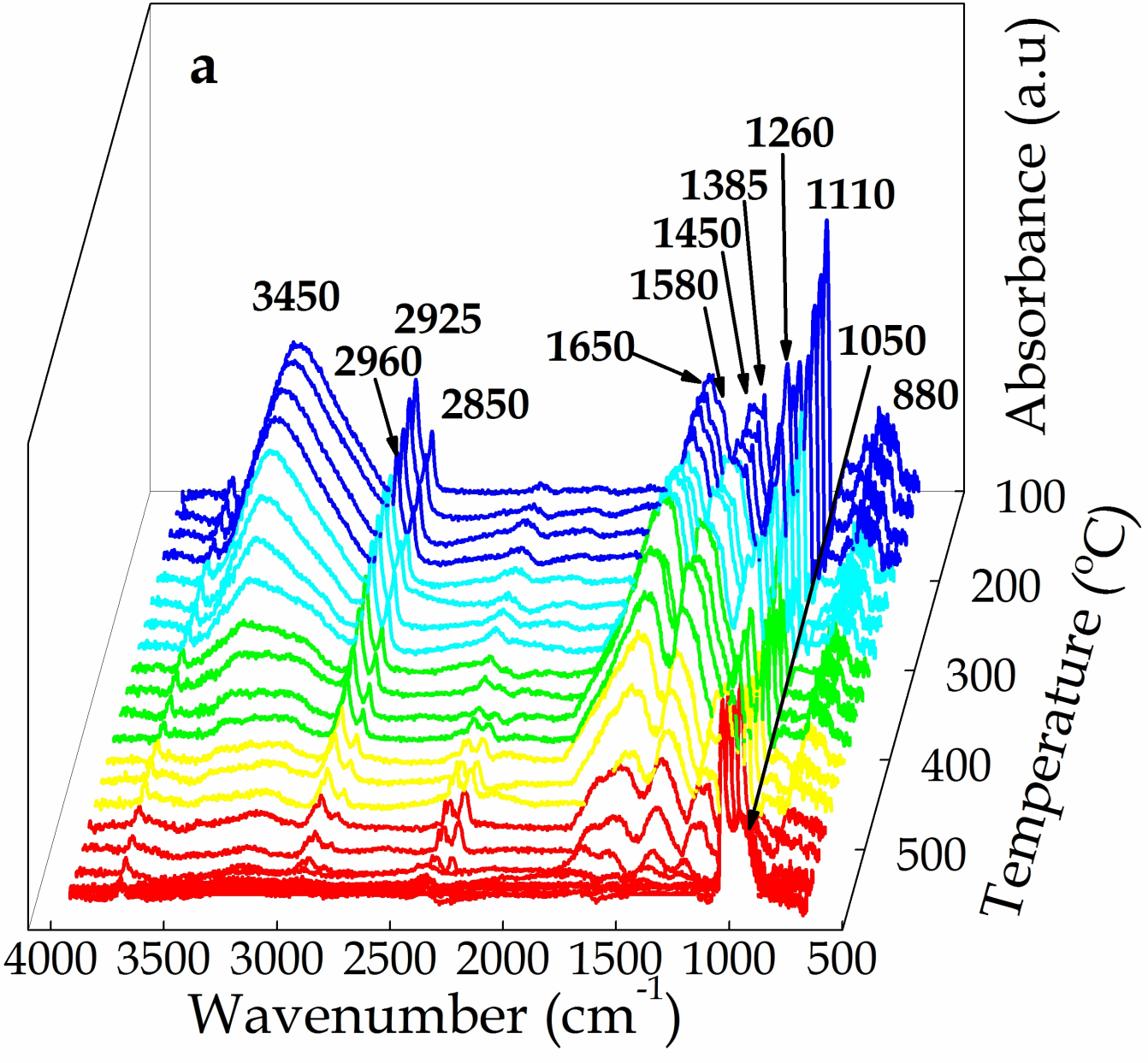
a
3450
2960
2925
2850
1650
1580
1450
1385
1260
1110
1050
880
Absorbance (a.u)
100
200
300
400
500
Temperature (°C)
4000 3500 3000 2500 2000 1500 1000 500
Wavenumber (cm-1)

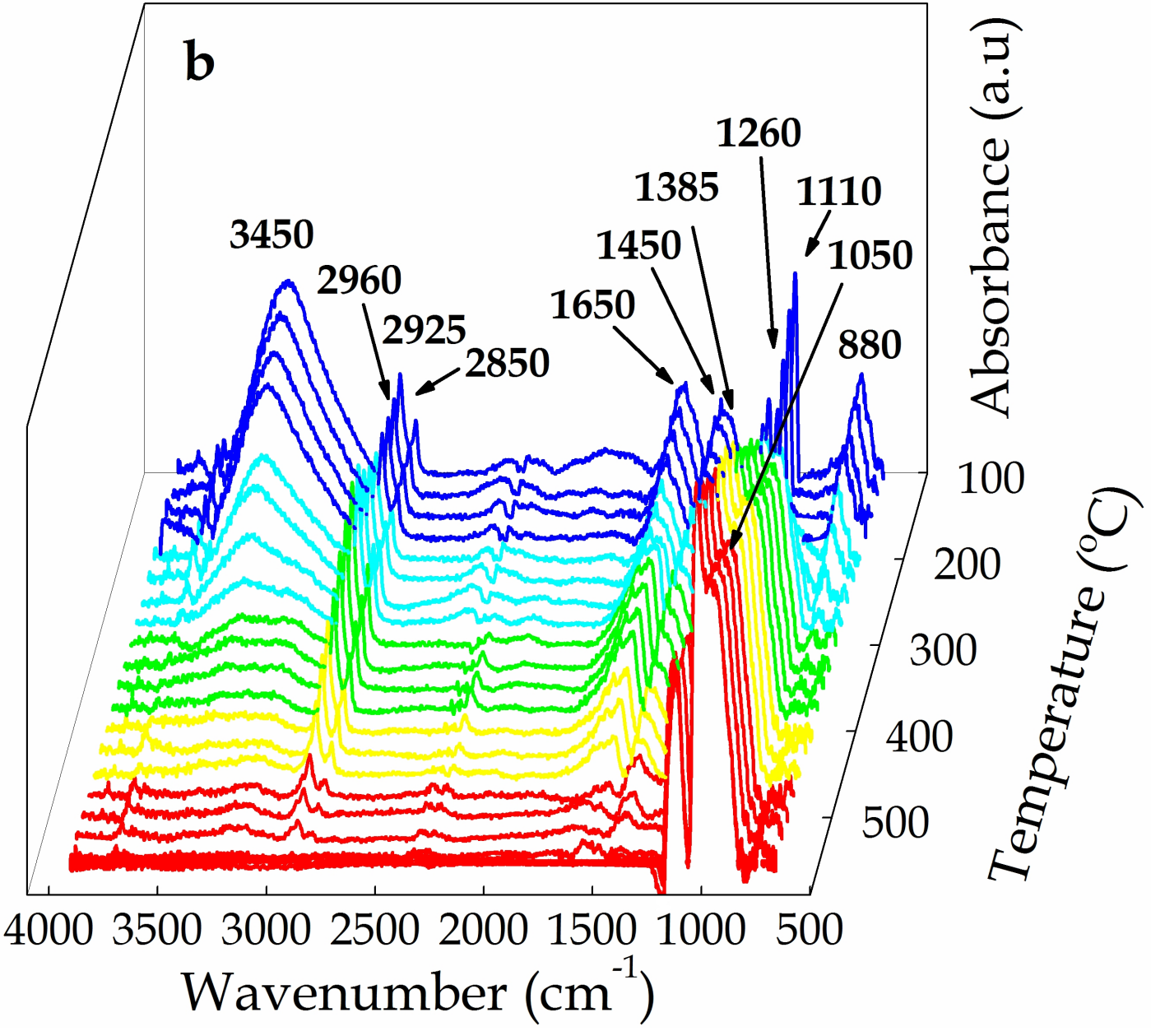
b
3450
2960
2925
2850
1650
1450
1385
1260
1110
1050
880
4000 3500 3000 2500 2000 1500 1000 500
Wavenumber (cm-1)
100
200
300
400
500
Temperature (°C)
Absorbance (a.u)

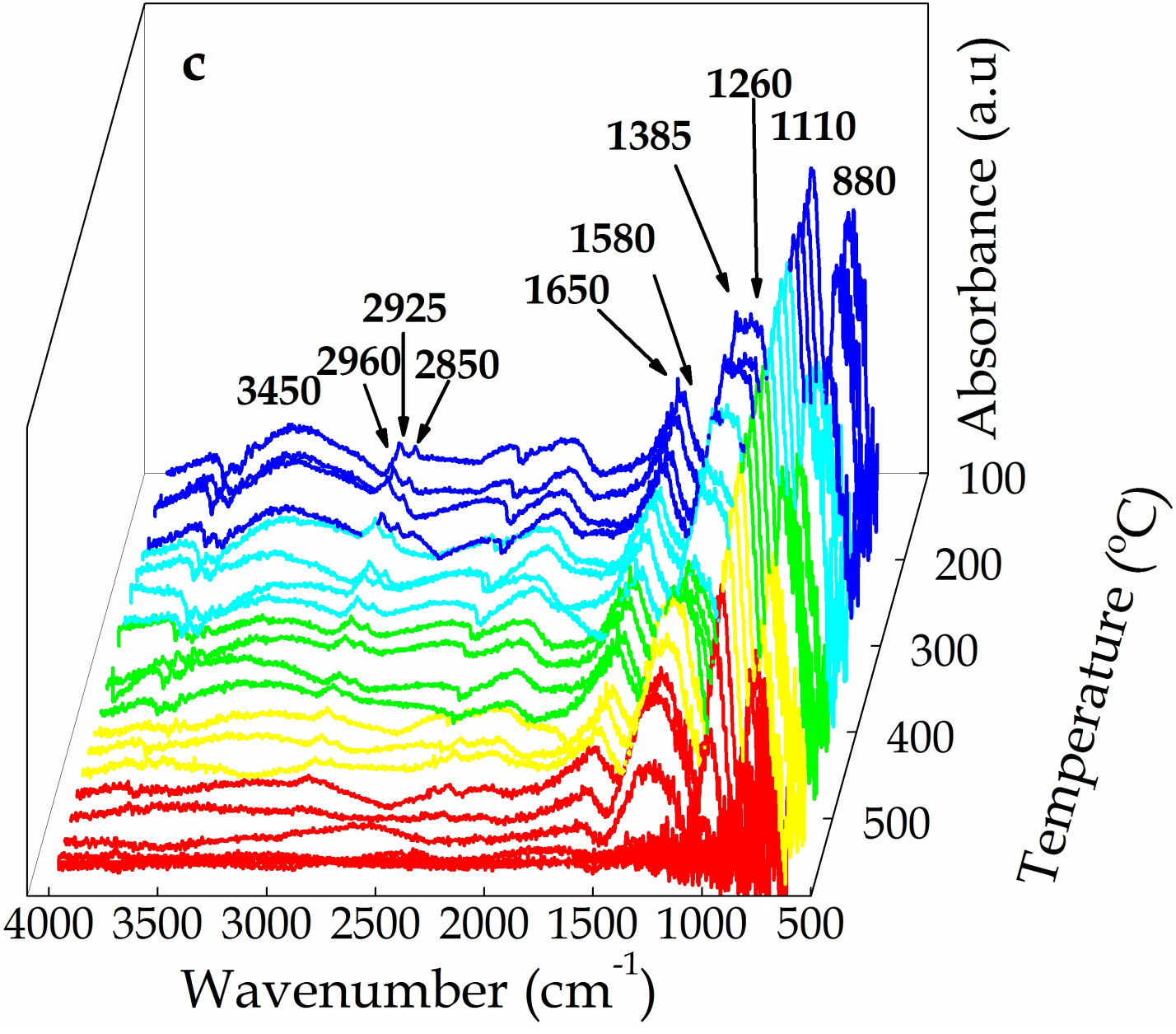
c
3450
2960
2925
2850
1650
1580
1385
1260
1110
880
Absorbance (a.u)
100
200
300
400
500
Temperature (°C)
4000 3500 3000 2500 2000 1500 1000 500
Wavenumber (cm-1)